Control of Parallel Manipulators

Dehaeze Thomas

April 11, 2025

Contents

When controlling a MIMO system (specifically parallel manipulator such as the Stewart platform?)

- ☐ **Should the quick review of Stewart platform control be here?** In that case it should be possible to highlight three areas:
  - use of multiple sensors
  - decoupling strategy
  - control optimization

Several considerations:

- Section 1: How to most effectively use/combine multiple sensors
- Section 2: How to decouple a system
- Section 3: How to design the controller

1 Multiple Sensor Control

The literature review of Stewart platforms revealed a wide diversity of designs with various sensor and actuator configurations. Control objectives (such as active damping, vibration isolation, or precise positioning) dictate specific sensor configurations. The selection between inertial sensors, force sensors, or relative position sensors is primarily determined by the system's control requirements.

In cases where multiple control objectives must be achieved simultaneously, as is the case for the Nano Active Stabilization System (NASS) where the Stewart platform must both position the sample and provide isolation from micro-station vibrations, combining multiple sensors within the control architecture has been demonstrated to yield significant performance benefits. From the literature, three principal approaches for combining sensors have been identified: High Authority Control-Low Authority Control (HAC-LAC), sensor fusion, and two-sensor control architectures.

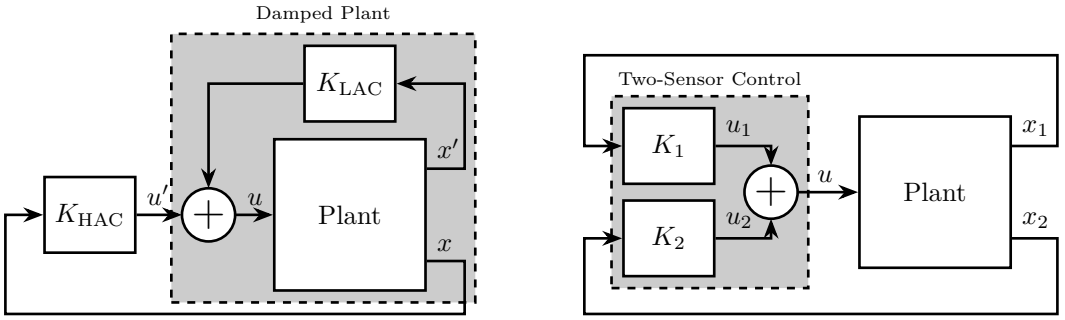

(a) HAC LAC

(b) Two Sensor Control

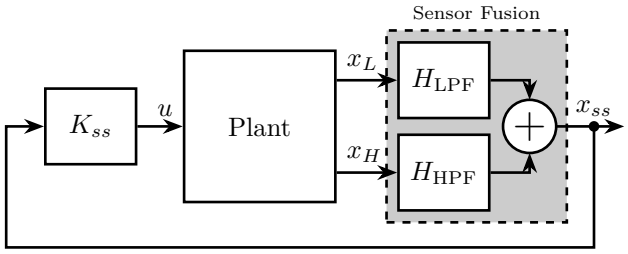

(c) Sensor Fusion

Figure 1.1: Different control strategies when using multiple sensors. High Authority Control / Low Authority Control (a). Sensor Fusion (c). Two-Sensor Control (b)

The HAC-LAC approach, implemented during the conceptual phase, employs a dual-loop control strategy in which two control loops utilize different sensors for distinct purposes (Figure 1.1a). In [1], vibration isolation is provided by accelerometers collocated with the voice coil actuators, while external rotational sensors are utilized to achieve pointing control. In [2], force sensors collocated with

the magnetostrictive actuators are used for active damping using decentralized IFF, and subsequently accelerometers are employed for adaptive vibration isolation. Similarly, in [3], piezoelectric actuators with collocated force sensors are used in a decentralized manner to provide active damping while accelerometers are implemented in an adaptive feedback loop to suppress periodic vibrations. In [4], force sensors are integrated in the struts for decentralized force feedback while accelerometers fixed to the top platform are employed for centralized control.

The second approach, sensor fusion (illustrated in Figure 1.1c), involves filtering signals from two sensors using complementary filters[1] and summing them to create an improved sensor signal. In [5], geophones (used at low frequency) are merged with force sensors (used at high frequency). It is demonstrated that combining both sensors using sensor fusion can improve performance compared to using the individual sensors independently. In [6], sensor fusion architecture is implemented with an accelerometer and a force sensor. This implementation is shown to simultaneously achieve high damping of structural modes (through the force sensors) while maintaining very low vibration transmissibility (through the accelerometers).

In [7], the performance of sensor fusion is compared with the more general case of "two-sensor control" (illustrated in Figure 1.1b). It is highlighted that "two-sensor control" provides greater control freedom, potentially enhancing performance. In [8], the use of force sensors and geophones is compared for vibration isolation purposes. Geophones are shown to provide better isolation performance than load cells but suffer from poor robustness. Conversely, the controller based on force sensors exhibited inferior performance (due to the presence of a pair of low frequency zeros), but demonstrated better robustness properties. A "two-sensor control" approach was proven to perform better than controllers based on individual sensors while maintaining better robustness. A Linear Quadratic Regulator (LQG) was employed to optimize the two-input/one-output controller.

Beyond these three main approaches, other control architectures have been proposed for different purposes. In [9], a first control loop utilizes force sensors and relative motion sensors to compensate for parasitic stiffness of the flexible joints. Subsequently, the system is decoupled in the modal space (facilitated by the removal of parasitic stiffness) and accelerometers are employed for vibration isolation.

The HAC-LAC architecture was previously investigated during the conceptual phase and successfully implemented to validate the NASS concept, demonstrating excellent performance. At the other end of the spectrum, the two-sensor approach yields greater control design freedom but introduces increased complexity in tuning, and thus was not pursued in this study. This work instead focuses on sensor fusion, which represents a promising middle ground between the proven HAC-LAC approach and the more complex two-sensor control strategy.

A review of sensor fusion is first presented (Section 1.1), followed by an examination of the fundamental theoretical concepts (Section 1.2). In this section, both the robustness of the fusion and the noise characteristics of the resulting "super sensor" are derived and expressed as functions of the complementary filters' norms. A synthesis method for designing complementary filters that allow to shape their norms is proposed (Section 1.3). The investigation is then extended beyond the conventional two-sensor scenario, demonstrating how the proposed complementary filter synthesis can be generalized for applications requiring the fusion of three or more sensors (Section 1.4).

[1] A set of two complementary filters are two transfer functions that sum to one.

1.1 Review of Sensor Fusion

Sensors used to measure physical quantities have two primary limitations: measurement accuracy which is compromised by various noise sources (including electrical noise from conditioning electronics), and limited measurement bandwidth. Sensor fusion offers a solution to these limitations by combining multiple sensors [10]. By strategically selecting sensors with complementary characteristics, a "super sensor" can be created that combines the advantages of each individual sensor.

Measuring a physical quantity using sensors is always subject to several limitations. First, the accuracy of the measurement is affected by various noise sources, such as electrical noise from the conditioning electronics. Second, the frequency range in which the measurement is relevant is bounded by the bandwidth of the sensor. One way to overcome these limitations is to combine several sensors using a technique called "sensor fusion" [10]. Fortunately, a wide variety of sensors exists, each with different characteristics. By carefully selecting the sensors to be fused, a "super sensor" is obtained that combines the benefits of the individual sensors.

In some applications, sensor fusion is employed to increase measurement bandwidth [11], [12], [13]. For instance, in [11], the bandwidth of a position sensor is extended by fusing it with an accelerometer that provides high-frequency motion information. In other applications, sensor fusion is utilized to obtain an estimate of the measured quantity with reduced noise [14], [15], [16], [17]. More recently, the fusion of sensors measuring different physical quantities has been proposed to enhance control properties [18], [19]. In [18], an inertial sensor used for active vibration isolation is fused with a sensor collocated with the actuator to improve the stability margins of the feedback controller.

On top of Stewart platforms, practical applications of sensor fusion are numerous. It is widely implemented for attitude estimation in autonomous vehicles such as unmanned aerial vehicles [20], [21], [22] and underwater vehicles [23], [24]. Sensor fusion offers significant benefits for high-performance positioning control as demonstrated in [11], [12], [13], [19]. It has also been identified as a key technology for improving the performance of active vibration isolation systems [6]. Emblematic examples include the isolation stages of gravitational wave detectors [18], [25] such as those employed at LIGO [14], [15] and Virgo [26].

Two principal methods are employed to perform sensor fusion: using complementary filters [27] or using Kalman filtering [28]. For sensor fusion applications, these methods share many relationships [17], [28], [29], [30]. However, Kalman filtering requires assumptions about the probabilistic characteristics of sensor noise [17], whereas complementary filters do not impose such requirements. Furthermore, complementary filters offer advantages over Kalman filtering for sensor fusion through their general applicability, low computational cost [29], and intuitive nature, as their effects can be readily interpreted in the frequency domain.

A set of filters is considered complementary if the sum of their transfer functions equals one at all frequencies. In early implementations of complementary filtering, analog circuits were used to physically realize the filters [27]. While analog complementary filters remain in use today [19], [31], digital implementation is now more common as it provides greater flexibility.

Various design methods have been developed to optimize complementary filters. The most straightforward approach utilizes analytical formulas. Depending on the application, these formulas may be of first order [19], [21], [32], second order [20], [22], [33], or higher orders [11], [12], [18], [33], [34].

Since the characteristics of the super sensor depend on the proper design of complementary filters [35], several optimization techniques have been developed. Some approaches focus on finding optimal parameters for analytical formulas [13], [22], [30], while others employ convex optimization tools [14],

[15] such as linear matrix inequalities [23]. As demonstrated in [16], complementary filter design can be linked to the standard mixed-sensitivity control problem. Consequently, the powerful tools developed for classical control theory can be applied to complementary filter design. For example, in [22], the two gains of a Proportional Integral (PI) controller are optimized to minimize super sensor noise.

All these complementary filter design methods share the common objective of creating a super sensor with desired characteristics, typically in terms of noise and dynamics. As reported in [12], [16], phase shifts and magnitude bumps in the super sensor dynamics may occur if complementary filters are poorly designed or if sensors are improperly calibrated. Therefore, the robustness of the fusion must be considered when designing complementary filters. Despite the numerous design methods proposed in the literature, a simple approach that specifies desired super sensor characteristics while ensuring good fusion robustness has been lacking.

Fortunately, both fusion robustness and super sensor characteristics can be linked to complementary filter magnitude [35]. Based on this relationship, the present work introduces an approach to designing complementary filters using $\mathcal{H}_\infty$ synthesis, which enables intuitive shaping of complementary filter magnitude in a straightforward manner.

1.2 Sensor Fusion and Complementary Filters Requirements

A general sensor fusion architecture using complementary filters is shown in Figure 1.2, where multiple sensors (in this case two) measure the same physical quantity x. The sensor output signals $\hat{x}_1$ and $\hat{x}_2$ represent estimates of x. These estimates are filtered by complementary filters and combined to form a new estimate $\hat{x}$.

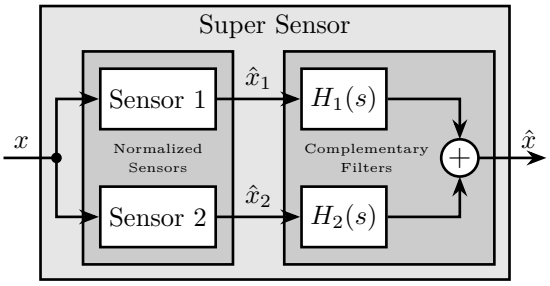

Figure 1.2: Schematic of a sensor fusion architecture using complementary filters.

The complementary property of filters $H_1(s)$ and $H_2(s)$ requires that the sum of their transfer functions equals one at all frequencies (1.1).

$$H_1(s) + H_2(s) = 1 \tag{1.1}$$

Sensor Models and Sensor Normalization To analyze sensor fusion architectures, appropriate sensor models are required. The model shown in Figure 1.3a consists of a linear time invariant (LTI) system $G_i(s)$ representing the sensor dynamics and an input n_i representing sensor noise. The model input x is the measured physical quantity, and its output $\tilde{x}_i$ is the "raw" output of the sensor.

Prior to filtering the sensor outputs $\tilde{x}_i$ with complementary filters, the sensors are typically normalized to simplify the fusion process. This normalization involves using an estimate $\hat{G}_i(s)$ of the sensor dynamics

$G_i(s)$, and filtering the sensor output by the inverse of this estimate $\hat{G}_i^{-1}(s)$, as shown in Figure 1.3b. It is assumed that the sensor inverse $\hat{G}_i^{-1}(s)$ is proper and stable. This approach ensures that the units of the estimates $\hat{x}_i$ match the units of the physical quantity x. The sensor dynamics estimate $\hat{G}_i(s)$ may be a simple gain or a more complex transfer function.

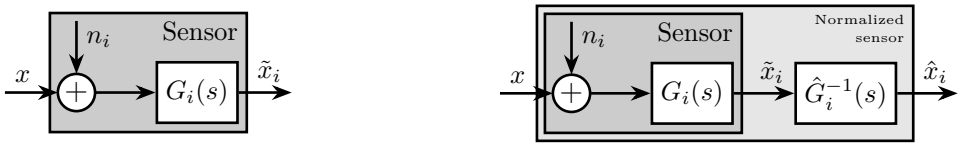

(a) Basic sensor model consisting of a noise input n_i and a linear time invariant transfer function $G_i(s)$

(b) Normalized sensors using the inverse of an estimate $\hat{G}$

Figure 1.3: Sensor models with and without normalization.

Two normalized sensors are then combined to form a super sensor as shown in Figure 1.4. The two sensors measure the same physical quantity x with dynamics $G_1(s)$ and $G_2(s)$, and with uncorrelated noises n_1 and n_2. The signals from both normalized sensors are fed into two complementary filters $H_1(s)$ and $H_2(s)$ and then combined to yield an estimate $\hat{x}$ of x. The super sensor output $\hat{x}$ is therefore described by (1.2).

$$\hat{x} = \Big(H_1(s)\hat{G}_1^{-1}(s)G_1(s) + H_2(s)\hat{G}_2^{-1}(s)G_2(s)\Big)x + H_1(s)\hat{G}_1^{-1}(s)G_1(s)n_1 + H_2(s)\hat{G}_2^{-1}(s)G_2(s)n_2 \quad (1.2)$$

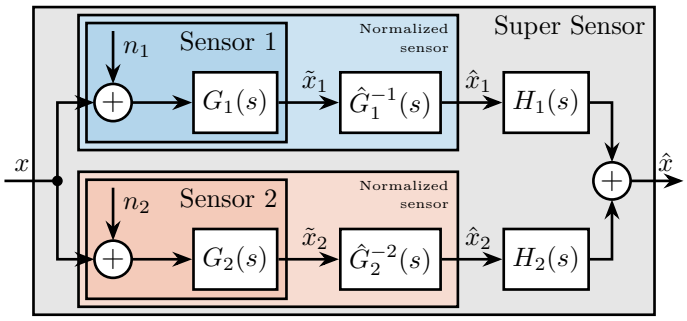

Figure 1.4: Sensor fusion architecture with two normalized sensors.

Noise Sensor Filtering First, consider the case where all sensors are perfectly normalized (1.3). The effects of imperfect normalization will be addressed subsequently.

$$\frac{\hat{x}_i}{x} = \hat{G}_i(s)G_i(s) = 1 \quad (1.3)$$

In that case, the super sensor output $\hat{x}$ equals x plus the filtered noise from both sensors (1.4). From this equation, it is evident that the complementary filters $H_1(s)$ and $H_2(s)$ operate solely on the sensor noise. Thus, this sensor fusion architecture allows filtering of sensor noise without introducing distortion in the measured physical quantity. This fundamental property necessitates that the two filters must be complementary.

$$\hat{x} = x + H_1(s)n_1 + H_2(s)n_2 \tag{1.4}$$

The estimation error ϵ_x, defined as the difference between the sensor output $\hat{x}$ and the measured quantity x, is computed for the super sensor (1.5).

$$\epsilon_x \triangleq \hat{x} - x = H_1(s)n_1 + H_2(s)n_2 \tag{1.5}$$

As shown in (1.6), the Power Spectral Density (PSD) of the estimation error Φ_{ϵ_x} depends both on the norm of the two complementary filters and on the PSD of the noise sources Φ_{n_1} and Φ_{n_2}.

$$\Phi_{\epsilon_x}(\omega) = |H_1(j\omega)|^2 \Phi_{n_1}(\omega) + |H_2(j\omega)|^2 \Phi_{n_2}(\omega) \tag{1.6}$$

If the two sensors have identical noise characteristics ($\Phi_{n_1}(\omega) = \Phi_{n_2}(\omega)$), simple averaging ($H_1(s) = H_2(s) = 0.5$) would minimize the super sensor noise. This represents the simplest form of sensor fusion using complementary filters.

However, sensors typically exhibit high noise levels in different frequency regions. In such cases, to reduce the noise of the super sensor, the norm $|H_1(j\omega)|$ should be minimized when $\Phi_{n_1}(\omega)$ exceeds $\Phi_{n_2}(\omega)$, and the norm $|H_2(j\omega)|$ should be minimized when $\Phi_{n_2}(\omega)$ exceeds $\Phi_{n_1}(\omega)$. Therefore, by appropriately shaping the norm of the complementary filters, the noise of the super sensor can be minimized.

Sensor Fusion Robustness In practical systems, sensor normalization is rarely perfect, and condition (1.3) is not fully satisfied.

To analyze such imperfections, a multiplicative input uncertainty is incorporated into the sensor dynamics (Figure 1.5a). The nominal model is the estimated model used for normalization $\hat{G}_i(s)$, $\Delta_i(s)$ is any stable transfer function satisfying $|\Delta_i(j\omega)| \leq 1$, $\forall\omega$, and $w_i(s)$ is a weighting transfer function representing the magnitude of uncertainty. The weight $w_i(s)$ is selected such that the actual sensor dynamics $G_i(j\omega)$ remains within the uncertain region represented by a circle in the complex plane, centered on 1 with a radius equal to $|w_i(j\omega)|$.

Since the nominal sensor dynamics is taken as the normalized filter, the normalized sensor model can be further simplified as shown in Figure 1.5b.

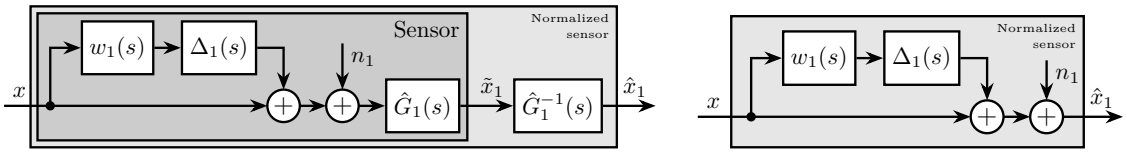

(a) Sensor with multiplicative input uncertainty

(b) Simplified sensor model

Figure 1.5: Sensor models with dynamical uncertainty

The sensor fusion architecture incorporating sensor models with dynamical uncertainty is illustrated in Figure 1.6a. The super sensor dynamics (1.7) is no longer unity but depends on the sensor dynamical

uncertainty weights $w_i(s)$ and the complementary filters $H_i(s)$. The dynamical uncertainty of the super sensor can be graphically represented in the complex plane by a circle centered on 1 with a radius equal to $|w_1(j\omega)H_1(j\omega)| + |w_2(j\omega)H_2(j\omega)|$ (Figure 1.6b).

The sensor fusion architecture with the sensor models including dynamical uncertainty is shown in Figure 1.6a. The super sensor dynamics (1.7) is no longer equal to 1 and now depends on the sensor dynamical uncertainty weights $w_i(s)$ as well as on the complementary filters $H_i(s)$. The dynamical uncertainty of the super sensor can be graphically represented in the complex plane by a circle centered on 1 with a radius equal to $|w_1(j\omega)H_1(j\omega)| + |w_2(j\omega)H_2(j\omega)|$ (Figure 1.6b).

$$\frac{\hat{x}}{x} = 1 + w_1(s)H_1(s)\Delta_1(s) + w_2(s)H_2(s)\Delta_2(s) \tag{1.7}$$

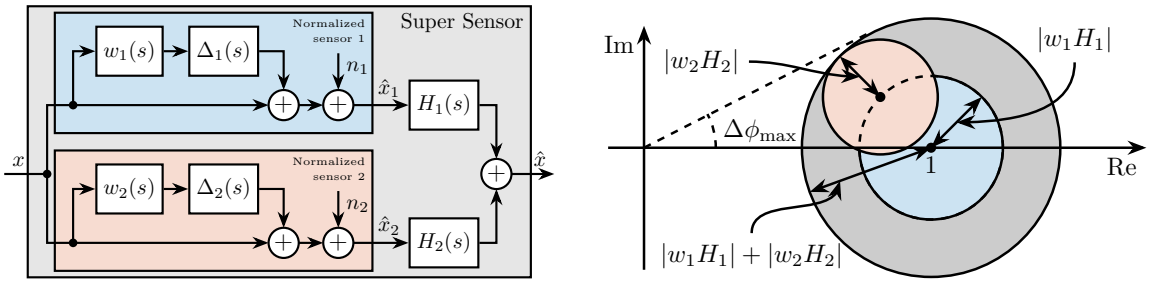

(a) Sensor Fusion Architecture

(b) Uncertainty regions

Figure 1.6: Sensor fusion architecture with sensor dynamics uncertainty (a). Uncertainty region (b) of the super sensor dynamics in the complex plane (grey circle). The contribution of both sensors 1 and 2 to the total uncertainty are represented respectively by a blue circle and a red circle. The frequency dependency ω is here omitted.

The super sensor dynamical uncertainty, and consequently the robustness of the fusion, clearly depends on the complementary filters' norm. As it is generally desired to limit the dynamical uncertainty of the super sensor, the norm of the complementary filter $|H_i(j\omega)|$ should be made small when $|w_i(j\omega)|$ is large, i.e., at frequencies where the sensor dynamics is uncertain.

1.3 Complementary Filters Shaping

As established in Section 1.2, the super sensor's noise characteristics and robustness are directly dependent on the complementary filters' norm. A synthesis method enabling precise shaping of these norms would therefore offer substantial practical benefits. This section develops such an approach by formulating the design objective as a standard $\mathcal{H}_\infty$ optimization problem. The methodology for designing appropriate weighting functions (which specify desired complementary filter shapes during synthesis) is examined in detail, and the efficacy of the proposed method is validated with a simple example.

Synthesis Objective The primary objective is to shape the norms of two filters $H_1(s)$ and $H_2(s)$ while ensuring they maintain their complementary property as defined in (1.1). This is equivalent to finding proper and stable transfer functions $H_1(s)$ and $H_2(s)$ that satisfy conditions (1.8a), (1.8b), and (1.8c). Weighting transfer functions $W_1(s)$ and $W_2(s)$ are strategically selected to define the maximum desired norm of the complementary filters during the synthesis process.

$$H_1(s) + H_2(s) = 1 \tag{1.8a}$$

$$|H_1(j\omega)| \leq \frac{1}{|W_1(j\omega)|} \quad \forall\omega \tag{1.8b}$$

$$|H_2(j\omega)| \leq \frac{1}{|W_2(j\omega)|} \quad \forall\omega \tag{1.8c}$$

Shaping of Complementary Filters using $\mathcal{H}_\infty$ synthesis The synthesis objective can be readily expressed as a standard $\mathcal{H}_\infty$ optimization problem and solved using widely available computational tools. Consider the generalized plant $P(s)$ illustrated in Figure 1.7a and mathematically described by (1.9).

$$\begin{bmatrix} z_1 \\ z_2 \\ v \end{bmatrix} = P(s) \begin{bmatrix} w \\ u \end{bmatrix}; \quad P(s) = \begin{bmatrix} W_1(s) & -W_1(s) \\ 0 & W_2(s) \\ 1 & 0 \end{bmatrix} \tag{1.9}$$

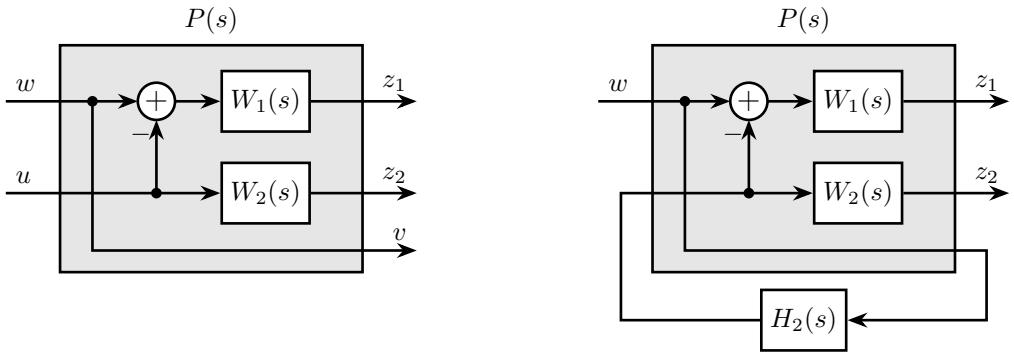

(a) Generalized plant **(b)** Generalized plant with the synthesized filter

Figure 1.7: Architecture for the $\mathcal{H}_\infty$ synthesis of complementary filters

Applying standard $\mathcal{H}_\infty$ synthesis to the generalized plant $P(s)$ is equivalent to finding a stable filter $H_2(s)$ that, based on input v, generates an output signal u such that the $\mathcal{H}_\infty$ norm of the system shown in Figure 1.7b from w to $[z_1,\ z_2]$ does not exceed unity, as expressed in (1.10).

$$\left\| \begin{matrix} (1 - H_2(s))\, W_1(s) \\ H_2(s) W_2(s) \end{matrix} \right\|_\infty \leq 1 \tag{1.10}$$

By defining $H_1(s)$ as the complement of $H_2(s)$ ((1.11)), the $\mathcal{H}_\infty$ synthesis objective becomes equivalent to (1.12), ensuring that conditions (1.8b) and (1.8c) are satisfied.

$$H_1(s) \triangleq 1 - H_2(s) \tag{1.11}$$

$$\left\| \begin{matrix} H_1(s) W_1(s) \\ H_2(s) W_2(s) \end{matrix} \right\|_\infty \leq 1 \tag{1.12}$$

Therefore, applying $\mathcal{H}_\infty$ synthesis to the standard plant $P(s)$ ((1.9)) generates two filters, $H_2(s)$ and $H_1(s) \triangleq 1 - H_2(s)$, that are complementary as required by (1.8), with norms bounded by the specified constraints in (1.8b) and (1.8c).

It should be noted that there exists only an implication (not an equivalence) between the $\mathcal{H}_\infty$ norm condition in (1.12) and the initial synthesis objectives in (1.8b) and (1.8c). Consequently, the optimization may be somewhat conservative with respect to the set of filters on which it operates (see [36, Chap. 2.8.3]).

Weighting Functions Design Weighting functions play a crucial role during synthesis by specifying the maximum allowable norms for the complementary filters. The proper design of these weighting functions is essential for the successful implementation of the proposed $\mathcal{H}_\infty$ synthesis approach.

Three key considerations should guide the design of weighting functions. First, only proper and stable transfer functions should be employed. Second, the order of the weighting functions should remain reasonably small to minimize computational costs associated with solving the optimization problem and to facilitate practical implementation of the filters (as the order of the synthesized filters equals the sum of the weighting functions' orders). Third, the fundamental limitations imposed by the complementary property ((1.1)) must be respected, which implies that $|H_1(j\omega)|$ and $|H_2(j\omega)|$ cannot both be made small at the same frequency.

When designing complementary filters, it is typically desirable to specify their slopes, "blending" frequency, and maximum gains at low and high frequencies. To facilitate the expression of these specifications, formula (1.13) is proposed for the design of weighting functions. The parameters in this formula are $G_0 = \lim_{\omega\to 0} |W(j\omega)|$ (the low-frequency gain), $G_\infty = \lim_{\omega\to\infty} |W(j\omega)|$ (the high-frequency gain), $G_c = |W(j\omega_c)|$ (the gain at a specific frequency ω_c in rad/s), and n (the slope between high and low frequency, which also corresponds to the order of the weighting function). The typical magnitude response of a weighting function generated using (1.13) is illustrated in Figure 1.8.

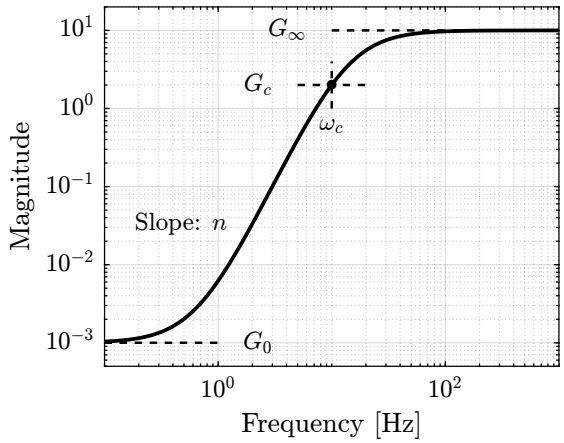

Figure 1.8: Magnitude of a weighting function generated using (1.13), $G_0 = 10^{-3}$, $G_\infty = 10$, $\omega_c = 10\,\text{Hz}$, $G_c = 2$, $n = 3$.

$$W(s) = \left(\frac{\frac{1}{\omega_c}\sqrt{\frac{1-\left(\frac{G_0}{G_c}\right)^{\frac{2}{n}}}{1-\left(\frac{G_c}{G_\infty}\right)^{\frac{2}{n}}}}\, s + \left(\frac{G_0}{G_c}\right)^{\frac{1}{n}}}{\left(\frac{1}{G_\infty}\right)^{\frac{1}{n}} \frac{1}{\omega_c}\sqrt{\frac{1-\left(\frac{G_0}{G_c}\right)^{\frac{2}{n}}}{1-\left(\frac{G_c}{G_\infty}\right)^{\frac{2}{n}}}}\, s + \left(\frac{1}{G_c}\right)^{\frac{1}{n}}} \right)^n \tag{1.13}$$

Validation of the proposed synthesis method The proposed methodology for designing complementary filters is now applied to a simple example. Consider the design of two complementary filters $H_1(s)$ and $H_2(s)$ with the following requirements:

- The blending frequency should be approximately 10 Hz
- The slope of $|H_1(j\omega)|$ should be $+2$ below 10 Hz, with a low-frequency gain of 10^{-3}
- The slope of $|H_2(j\omega)|$ should be -3 above 10 Hz, with a high-frequency gain of 10^{-3}

The first step involves translating these requirements by appropriately designing the weighting functions. The formula proposed in (1.13) is employed for this purpose. The parameters used are summarized in Table 1.1. The inverse magnitudes of the designed weighting functions, which represent the maximum allowable norms of the complementary filters, are depicted by the dashed lines in Figure 1.9.

Parameter	$W_1(s)$	$W_2(s)$
G_0	0.1	1000
G_∞	1000	0.1
ω_c	$2\pi \cdot 10$	$2\pi \cdot 10$
G_c	0.45	0.45
n	2	3

Table 1.1: Parameters for $W_1(s)$ and $W_2(s)$

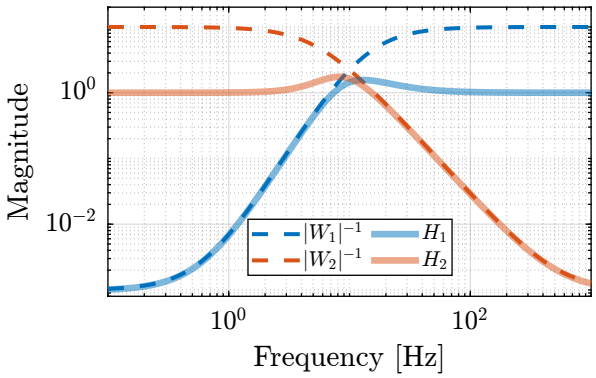

Figure 1.9: Weights and obtained filters

Standard $\mathcal{H}_\infty$ synthesis is then applied to the generalized plant shown in Figure 1.7a. This yields the filter $H_2(s)$ that minimizes the $\mathcal{H}_\infty$ norm from input w to outputs $[z_1,\ z_2]^\intercal$. The resulting $\mathcal{H}_\infty$ norm is found to be close to unity, indicating successful synthesis: the norms of the complementary filters remain below the specified upper bounds. This is confirmed by the Bode plots of the obtained complementary filters in Figure 1.9. This straightforward example demonstrates that the proposed methodology for shaping complementary filters is both simple and effective.

1.4 Synthesis of a set of three complementary filters

Certain applications necessitate the fusion of more than two sensors [30], [33]. At LIGO, for example, a super sensor is formed by merging three distinct sensors: an LVDT, a seismometer, and a geophone [34].

For merging $n > 2$ sensors with complementary filters, two architectural approaches are possible, as illustrated in Figure 1.10. Fusion can be implemented either "sequentially," utilizing $n-1$ sets of two complementary filters (Figure 1.10a), or "in parallel," employing a single set of n complementary filters (Figure 1.10b).

While conventional sensor fusion synthesis techniques can be applied to the sequential approach, parallel architecture implementation requires a novel synthesis method for multiple complementary filters. Previous literature has offered only simple analytical formulas for this purpose [30], [33]. This section presents a generalization of the proposed complementary filter synthesis method to address this gap.

The synthesis objective is to compute a set of n stable transfer functions $[H_1(s),\ H_2(s),\ \ldots,\ H_n(s)]$

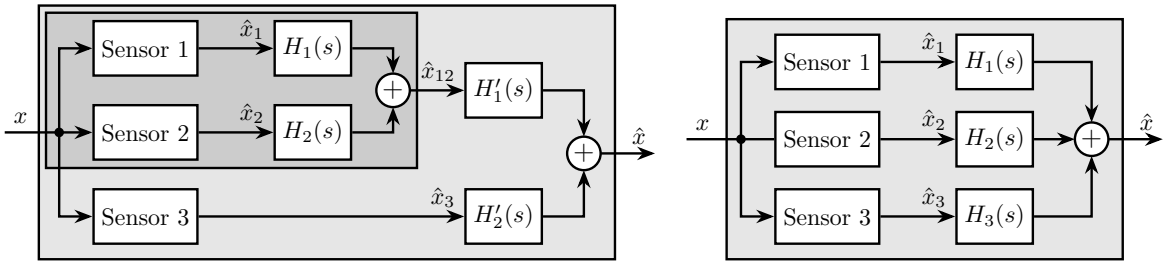

(a) Sequential fusion **(b)** Parallel fusion

Figure 1.10: Possible sensor fusion architecture when more than two sensors are to be merged

that satisfy conditions (1.14a) and (1.14b).

$$\sum_{i=1}^{n} H_i(s) = 1 \tag{1.14a}$$

$$|H_i(j\omega)| < \frac{1}{|W_i(j\omega)|}, \quad \forall\omega,\ i = 1 \dots n \tag{1.14b}$$

The transfer functions $[W_1(s),\ W_2(s),\ \dots,\ W_n(s)]$ are weights selected to specify the maximum complementary filters' norm during synthesis.

This synthesis objective is closely related to the one described in Section 1.3, and the proposed synthesis method represents a generalization of the approach previously presented. A set of n complementary filters can be shaped by applying standard $\mathcal{H}_\infty$ synthesis to the generalized plant $P_n(s)$ described by (1.15).

$$\begin{bmatrix} z_1 \\ \vdots \\ z_n \\ v \end{bmatrix} = P_n(s) \begin{bmatrix} w \\ u_1 \\ \vdots \\ u_{n-1} \end{bmatrix}; \quad P_n(s) = \begin{bmatrix} W_1 & -W_1 & \dots & \dots & -W_1 \\ 0 & W_2 & 0 & \dots & 0 \\ \vdots & \ddots & \ddots & \ddots & \vdots \\ \vdots & & \ddots & \ddots & 0 \\ 0 & \dots & \dots & 0 & W_n \\ 1 & 0 & \dots & \dots & 0 \end{bmatrix} \tag{1.15}$$

If the synthesis is successful, a set of $n-1$ filters $[H_2(s),\ H_3(s),\ \dots,\ H_n(s)]$ is obtained such that (1.16) is satisfied.

$$\left\| \begin{matrix} (1 - [H_2(s) + H_3(s) + \dots + H_n(s)])\, W_1(s) \\ H_2(s)W_2(s) \\ \vdots \\ H_n(s)W_n(s) \end{matrix} \right\|_\infty \leq 1 \tag{1.16}$$

$H_1(s)$ is then defined using (1.17), which ensures the complementary property for the set of n filters (1.14a). Condition (1.14b) is satisfied through (1.16).

$$H_1(s) \triangleq 1 - \left[H_2(s) + H_3(s) + \cdots + H_n(s)\right] \tag{1.17}$$

To validate the proposed method for synthesizing a set of three complementary filters, an example is provided. The sensors to be merged are a displacement sensor (effective from DC up to 1 Hz), a geophone (effective from 1 to 10 Hz), and an accelerometer (effective above 10 Hz). Three weighting functions are designed using formula (1.13), and their inverse magnitudes are shown in Figure 1.11b (dashed curves).

Consider the generalized plant $P_3(s)$ shown in Figure 1.11a, which is also described by (1.18).

$$\begin{bmatrix} z_1 \\ z_2 \\ z_3 \\ v \end{bmatrix} = P_3(s) \begin{bmatrix} w \\ u_1 \\ u_2 \end{bmatrix}; \quad P_3(s) = \begin{bmatrix} W_1(s) & -W_1(s) & -W_1(s) \\ 0 & W_2(s) & 0 \\ 0 & 0 & W_3(s) \\ 1 & 0 & 0 \end{bmatrix} \tag{1.18}$$

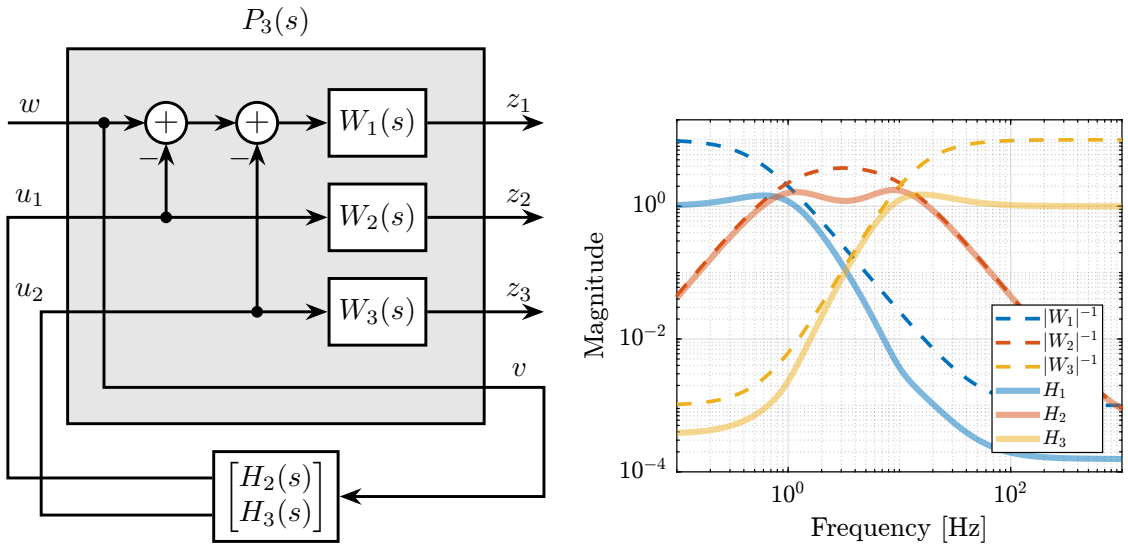

(a) Generalized plant with the synthesized filter

(b) Weights and obtained filters

Figure 1.11: Architecture for the $\mathcal{H}_\infty$ synthesis of three complementary filters (a). Bode plot of the inverse weighting functions and of the three obtained complementary filters (b)

Standard $\mathcal{H}_\infty$ synthesis is performed on the generalized plant $P_3(s)$. Two filters, $H_2(s)$ and $H_3(s)$, are obtained such that the $\mathcal{H}_\infty$ norm of the closed-loop transfer from w to $[z_1,\ z_2,\ z_3]$ of the system in Figure 1.11a is less than one. Filter $H_1(s)$ is defined using (1.19), thus ensuring the complementary property of the obtained set of filters.

$$H_1(s) \triangleq 1 - \left[H_2(s) + H_3(s)\right] \tag{1.19}$$

Figure 1.11b displays the three synthesized complementary filters (solid lines), confirming the successful synthesis.

Conclusion

A new method for designing complementary filters using the $\mathcal{H}_\infty$ synthesis has been proposed. This approach allows shaping of the filter magnitudes through the use of weighting functions during synthesis. This capability is particularly valuable in practice since the characteristics of the super sensor are directly linked to the complementary filters' magnitude. Consequently, typical sensor fusion objectives can be effectively translated into requirements on the magnitudes of the filters.

For the Nano Active Stabilization System (NASS), the High Authority Control-Integral Force Feedback (HAC-IFF) strategy was found to perform well and to offer the advantages of being both intuitive to understand and straightforward to tune. Looking forward, it would be interesting to investigate how sensor fusion (particularly between the force sensor and external metrology) compares to the HAC-IFF approach in terms of performance and robustness.

2 Decoupling

The control of parallel manipulators (and any MIMO system in general) typically involves a two-step approach: first decoupling the plant dynamics using various strategies, which will be discussed in this section, followed by the application of SISO control for the decoupled plant (discussed in section 3).

When sensors are integrated within the struts, decentralized control may be applied, as the system is already well decoupled at low frequency. For instance, [37] implemented a system where each strut consists of piezoelectric stack actuators and eddy current displacement sensors, with separate PI controllers for each strut. A similar control architecture was proposed in [38] using strain gauge sensors integrated in each strut.

An alternative strategy involves decoupling the system in the Cartesian frame using Jacobian matrices. As demonstrated during the study of Stewart platform kinematics, Jacobian matrices can be utilized to map actuator forces to forces and torques applied on the top platform. This approach enables the implementation of controllers in a defined frame. It has been applied with various sensor types including force sensors [39], relative displacement sensors [40], and inertial sensors [1], [41]. The Cartesian frame in which the system is decoupled is typically chosen at the point of interest (i.e., where the motion is of interest) or at the center of mass.

Modal control represents another noteworthy decoupling strategy, wherein the "local" plant inputs and outputs are mapped to the modal space. In this approach, multiple SISO plants, each corresponding to a single mode, can be controlled independently. This decoupling strategy has been implemented for active damping applications [42], which is logical as it is often desirable to dampen specific modes. The strategy has also been employed in [43] for vibration isolation purposes using geophones, and in [9] using force sensors.

Another completely different strategy, is to use implement a multivariable control directly on the coupled system. $\mathcal{H}_\infty$ and μ-synthesis were applied to a Stewart platform model in [44]. In [4], decentralized force feedback was first applied, followed by $\mathcal{H}_2$ synthesis for vibration isolation based on accelerometers. $\mathcal{H}_\infty$ synthesis was also employed in [45] for active damping based on accelerometers. [8] compared $\mathcal{H}_\infty$ synthesis with decentralized control in the frame of the struts. Their experimental closed-loop results indicated that the $\mathcal{H}_\infty$ controller did not outperform the decentralized controller in the frame of the struts. These limitations were attributed to the model's poor ability to predict off-diagonal dynamics, which is crucial for $\mathcal{H}_\infty$ synthesis.

The purpose of this section is to compare several methods for the decoupling of parallel manipulators, an analysis that appears to be lacking in the literature. The analysis begins in Section 2.1 with the introduction of a simplified parallel manipulator model that serves as the foundation for evaluating various decoupling strategies. Sections 2.3 through 2.5 systematically examine three distinct approaches: Jacobian matrix decoupling, modal decoupling, and Singular Value Decomposition (SVD) decoupling, respectively. The comparative assessment of these three methodologies, along with concluding observations, is provided in Section 2.6.

2.1 Test Model

Instead of utilizing the Stewart platform for comparing decoupling strategies, a simplified parallel manipulator is employed to facilitate a more straightforward analysis. The system illustrated in Figure 2.1 is used for this purpose. It possesses three degrees of freedom (DoF) and incorporates three parallel struts. Being a fully parallel manipulator, it is therefore quite similar to the Stewart platform.

Two reference frames are defined within this model: frame $\{M\}$ with origin O_M at the center of mass of the solid body, and frame $\{K\}$ with origin O_K at the center of stiffness of the parallel manipulator.

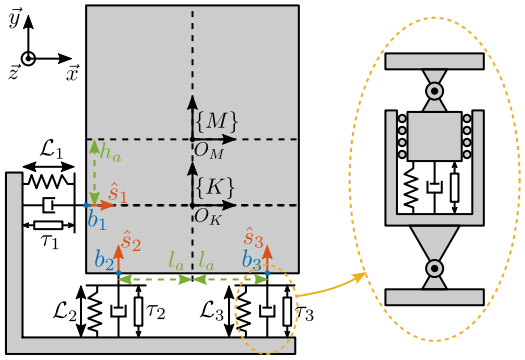

Figure 2.1: Model used to compare decoupling strategies

	Description	Value
l_a		$0.5\,m$
h_a		$0.2\,m$
k	Actuator stiffness	$10\,N/\mu m$
c	Actuator damping	$200\,Ns/m$
m	Payload mass	$40\,\mathrm{kg}$
I	Payload R_z inertia	$5\,\mathrm{kg}m^2$

Table 2.1: Model parameters

The equations of motion are derived by applying Newton's second law to the suspended mass, expressed at its center of mass (2.1), where $\boldsymbol{\mathcal{X}}_{\{M\}}$ represents the two translations and one rotation with respect to the center of mass, and $\boldsymbol{\mathcal{F}}_{\{M\}}$ denotes the forces and torque applied at the center of mass.

$$\boldsymbol{M}_{\{M\}}\ddot{\boldsymbol{\mathcal{X}}}_{\{M\}}(t) = \sum \boldsymbol{\mathcal{F}}_{\{M\}}(t), \quad \boldsymbol{\mathcal{X}}_{\{M\}} = \begin{bmatrix} x \\ y \\ R_z \end{bmatrix}, \quad \boldsymbol{\mathcal{F}}_{\{M\}} = \begin{bmatrix} F_x \\ F_y \\ M_z \end{bmatrix} \tag{2.1}$$

The Jacobian matrix $\boldsymbol{J}_{\{M\}}$ is employed to map the spring, damping, and actuator forces to XY forces and Z torque expressed at the center of mass (2.2).

$$\boldsymbol{J}_{\{M\}} = \begin{bmatrix} 1 & 0 & h_a \\ 0 & 1 & -l_a \\ 0 & 1 & l_a \end{bmatrix} \tag{2.2}$$

Subsequently, the equation of motion relating the actuator forces τ to the motion of the mass $\boldsymbol{\mathcal{X}}_{\{M\}}$ is derived (2.3).

$$\boldsymbol{M}_{\{M\}}\ddot{\boldsymbol{\mathcal{X}}}_{\{M\}}(t) + \boldsymbol{J}_{\{M\}}^{\intercal}\boldsymbol{\mathcal{C}}\boldsymbol{J}_{\{M\}}\dot{\boldsymbol{\mathcal{X}}}_{\{M\}}(t) + \boldsymbol{J}_{\{M\}}^{\intercal}\boldsymbol{\mathcal{K}}\boldsymbol{J}_{\{M\}}\boldsymbol{\mathcal{X}}_{\{M\}}(t) = \boldsymbol{J}_{\{M\}}^{\intercal}\boldsymbol{\tau}(t) \tag{2.3}$$

The matrices representing the payload inertia, actuator stiffness, and damping are shown in (2.4).

$$\boldsymbol{M}_{\{M\}} = \begin{bmatrix} m & 0 & 0 \\ 0 & m & 0 \\ 0 & 0 & I \end{bmatrix}, \quad \boldsymbol{\mathcal{K}} = \begin{bmatrix} k & 0 & 0 \\ 0 & k & 0 \\ 0 & 0 & k \end{bmatrix}, \quad \boldsymbol{\mathcal{C}} = \begin{bmatrix} c & 0 & 0 \\ 0 & c & 0 \\ 0 & 0 & c \end{bmatrix} \tag{2.4}$$

The parameters employed for the subsequent analysis are summarized in Table 2.1, which includes values for geometric parameters (l_a, h_a), mechanical properties (actuator stiffness k and damping c), and inertial characteristics (payload mass m and rotational inertia I).

2.2 Control in the frame of the struts

The dynamics in the frame of the struts are first examined. The equation of motion relating actuator forces $\boldsymbol{\tau}$ to strut relative motion $\boldsymbol{\mathcal{L}}$ is derived from equation (2.3) by mapping the Cartesian motion of the mass to the relative motion of the struts using the Jacobian matrix $\boldsymbol{J}_{\{M\}}$ defined in (2.2). The obtained transfer function from $\boldsymbol{\tau}$ to $\boldsymbol{\mathcal{L}}$ is shown in (2.5).

$$\frac{\boldsymbol{\mathcal{L}}}{\boldsymbol{\tau}}(s) = \boldsymbol{G}_{\mathcal{L}}(s) = \left(\boldsymbol{J}_{\{M\}}^{-\intercal} \boldsymbol{M}_{\{M\}} \boldsymbol{J}_{\{M\}}^{-1} s^2 + \boldsymbol{\mathcal{C}} s + \boldsymbol{\mathcal{K}} \right)^{-1} \tag{2.5}$$

At low frequencies, the plant converges to a diagonal constant matrix whose diagonal elements are related to the actuator stiffnesses (2.6). At high frequencies, the plant converges to the mass matrix mapped in the frame of the struts, which is generally highly non-diagonal.

$$\boldsymbol{G}_{\mathcal{L}}(j\omega) \xrightarrow[\omega \to 0]{} \boldsymbol{\mathcal{K}}^{-1} \tag{2.6}$$

The magnitude of the coupled plant $\boldsymbol{G}_{\mathcal{L}}$ is illustrated in Figure 2.2. This representation confirms that at low frequencies (below the first suspension mode), the plant is well decoupled. Depending on the symmetry present in the system, certain diagonal elements may exhibit identical values, as demonstrated for struts 2 and 3 in this example.

2.3 Jacobian Decoupling

Jacobian Matrix The Jacobian matrix serves a dual purpose in the decoupling process: it converts strut velocity $\dot{\mathcal{L}}$ to payload velocity and angular velocity $\dot{\boldsymbol{\mathcal{X}}}_{\{O\}}$, and it transforms actuator forces $\boldsymbol{\tau}$ to forces/torque applied on the payload $\boldsymbol{\mathcal{F}}_{\{O\}}$, as expressed in equation (2.7).

$$\dot{\boldsymbol{\mathcal{X}}}_{\{O\}} = \boldsymbol{J}_{\{O\}} \dot{\boldsymbol{\mathcal{L}}}, \quad \dot{\boldsymbol{\mathcal{L}}} = \boldsymbol{J}_{\{O\}}^{-1} \dot{\boldsymbol{\mathcal{X}}}_{\{O\}} \tag{2.7a}$$

$$\boldsymbol{\mathcal{F}}_{\{O\}} = \boldsymbol{J}_{\{O\}}^{\intercal} \boldsymbol{\tau}, \quad \boldsymbol{\tau} = \boldsymbol{J}_{\{O\}}^{-\intercal} \boldsymbol{\mathcal{F}}_{\{O\}} \tag{2.7b}$$

The resulting plant (Figure 2.3) have inputs and outputs with clear physical interpretations:

- $\boldsymbol{\mathcal{F}}_{\{O\}}$ represents forces/torques applied on the payload at the origin of frame $\{O\}$

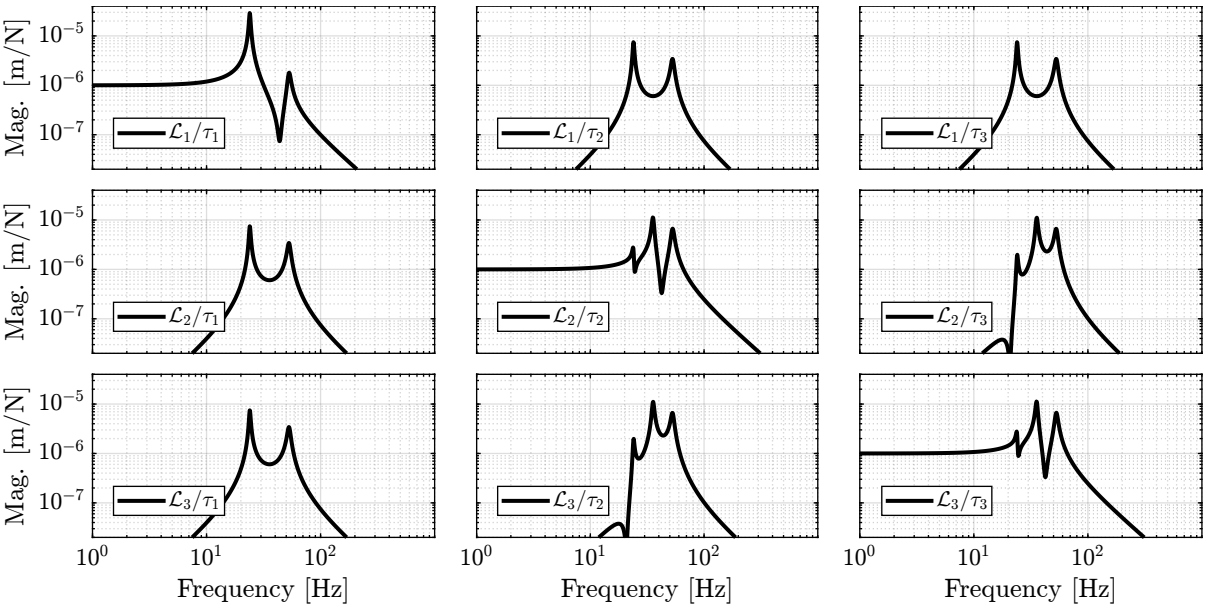

Figure 2.2: Model dynamics from actuator forces to relative displacement sensor of each strut.

- $\boldsymbol{\mathcal{X}}_{\{O\}}$ represents translations/rotation of the payload expressed in frame $\{O\}$

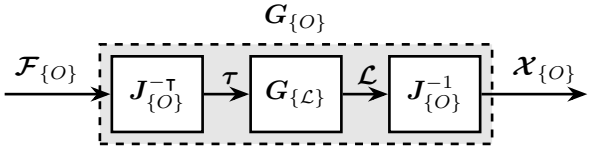

Figure 2.3: Block diagram of the transfer function from $\boldsymbol{\mathcal{F}}_{\{O\}}$ to $\boldsymbol{\mathcal{X}}_{\{O\}}$

The transfer function from $\boldsymbol{\mathcal{F}}_{\{O\}}$ to $\boldsymbol{\mathcal{X}}_{\{O\}}$, denoted $\boldsymbol{G}_{\{O\}}(s)$ can be computed using (2.8).

$$\frac{\boldsymbol{\mathcal{X}}_{\{O\}}}{\boldsymbol{\mathcal{F}}_{\{O\}}}(s) = \boldsymbol{G}_{\{O\}}(s) = \left(\boldsymbol{J}_{\{O\}}^{\intercal}\boldsymbol{J}_{\{M\}}^{-\intercal}\boldsymbol{M}_{\{M\}}\boldsymbol{J}_{\{M\}}^{-1}\boldsymbol{J}_{\{O\}}s^2 + \boldsymbol{J}_{\{O\}}^{\intercal}\boldsymbol{\mathcal{C}}\boldsymbol{J}_{\{O\}}s + \boldsymbol{J}_{\{O\}}^{\intercal}\boldsymbol{\mathcal{K}}\boldsymbol{J}_{\{O\}}\right)^{-1} \tag{2.8}$$

The frame $\{O\}$ can be selected according to specific requirements, but the decoupling properties are significantly influenced by this choice. Two natural reference frames are particularly relevant: the center of mass and the center of stiffness.

Center Of Mass When the decoupling frame is located at the center of mass (frame $\{M\}$ in Figure 2.1), the Jacobian matrix and its inverse are expressed as in (2.9).

$$\boldsymbol{J}_{\{M\}} = \begin{bmatrix} 1 & 0 & h_a \\ 0 & 1 & -l_a \\ 0 & 1 & l_a \end{bmatrix}, \quad \boldsymbol{J}_{\{M\}}^{-1} = \begin{bmatrix} 1 & \frac{h_a}{2l_a} & \frac{-h_a}{2l_a} \\ 0 & \frac{1}{2} & \frac{1}{2} \\ 0 & \frac{-1}{2l_a} & \frac{1}{2l_a} \end{bmatrix} \tag{2.9}$$

Analytical formula of the plant $\boldsymbol{G}_{\{M\}}(s)$ is derived (2.10).

$$\frac{\boldsymbol{\mathcal{X}}_{\{M\}}}{\boldsymbol{\mathcal{F}}_{\{M\}}}(s) = \boldsymbol{G}_{\{M\}}(s) = \left(\boldsymbol{M}_{\{M\}}s^2 + \boldsymbol{J}_{\{M\}}^\intercal \boldsymbol{\mathcal{C}} \boldsymbol{J}_{\{M\}} s + \boldsymbol{J}_{\{M\}}^\intercal \boldsymbol{\mathcal{K}} \boldsymbol{J}_{\{M\}}\right)^{-1} \tag{2.10}$$

At high frequencies, the plant converges to the inverse of the mass matrix, which is a diagonal matrix (2.11).

$$\boldsymbol{G}_{\{M\}}(j\omega) \xrightarrow[\omega\to\infty]{} -\omega^2 \boldsymbol{M}_{\{M\}}^{-1} = -\omega^2 \begin{bmatrix} 1/m & 0 & 0 \\ 0 & 1/m & 0 \\ 0 & 0 & 1/I \end{bmatrix} \tag{2.11}$$

Consequently, the plant exhibits effective decoupling at frequencies above the highest suspension mode as shown in Figure 2.4a. This strategy is typically employed in systems with low-frequency suspension modes [46], where the plant approximates decoupled mass lines.

The low-frequency coupling observed in this configuration has a clear physical interpretation. When a static force is applied at the center of mass, the suspended mass rotates around the center of stiffness. This rotation is due to torque induced by the stiffness of the first actuator (i.e. the one on the left side), which is not aligned with the force application point. This phenomenon is illustrated in Figure 2.4b.

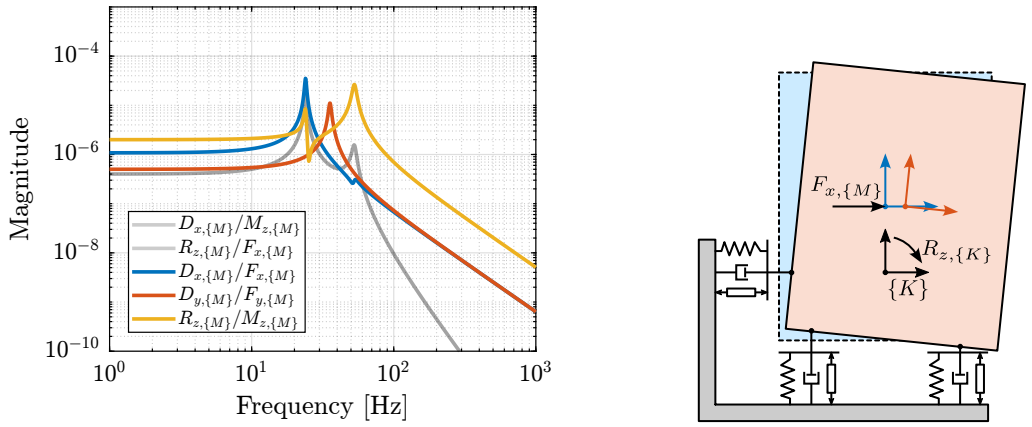

(a) Dynamics at the CoM

(b) Static force applied at the CoM

Figure 2.4: Plant decoupled using the Jacobian matrix expresssed at the center of mass (a). The physical reason for low frequency coupling is illustrated in (b).

Center Of Stiffness When the decoupling frame is located at the center of stiffness, the Jacobian matrix and its inverse are expressed as in (2.12).

$$\boldsymbol{J}_{\{K\}} = \begin{bmatrix} 1 & 0 & 0 \\ 0 & 1 & -l_a \\ 0 & 1 & l_a \end{bmatrix}, \quad \boldsymbol{J}_{\{K\}}^{-1} = \begin{bmatrix} 1 & 0 & 0 \\ 0 & \frac{1}{2} & \frac{1}{2} \\ 0 & \frac{-1}{2l_a} & \frac{1}{2l_a} \end{bmatrix} \tag{2.12}$$

The frame $\{K\}$ was selected based on physical reasoning, positioned in line with the side strut and equidistant between the two vertical struts. However, it could alternatively be determined through analytical methods to ensure that $\boldsymbol{J}_{\{K\}}^\intercal \boldsymbol{\mathcal{K}} \boldsymbol{J}_{\{K\}}$ forms a diagonal matrix. It should be noted that the

existence of such a center of stiffness (i.e. a frame $\{K\}$ for which $\boldsymbol{J}_{\{K\}}^{\intercal}\boldsymbol{\mathcal{K}}\boldsymbol{J}_{\{K\}}$ is diagonal) is not guaranteed for arbitrary systems. This property is typically achievable only in systems exhibiting specific symmetrical characteristics, as is the case in the present example.

The analytical expression for the plant in this configuration was then computed 2.13.

$$\frac{\boldsymbol{\mathcal{X}}_{\{K\}}}{\boldsymbol{\mathcal{F}}_{\{K\}}}(s) = \boldsymbol{G}_{\{K\}}(s) = \left(\boldsymbol{J}_{\{K\}}^{\intercal}\boldsymbol{J}_{\{M\}}^{-\intercal}\boldsymbol{M}_{\{M\}}\boldsymbol{J}_{\{M\}}^{-1}\boldsymbol{J}_{\{K\}}s^2 + \boldsymbol{J}_{\{K\}}^{\intercal}\boldsymbol{\mathcal{C}}\boldsymbol{J}_{\{K\}}s + \boldsymbol{J}_{\{K\}}^{\intercal}\boldsymbol{\mathcal{K}}\boldsymbol{J}_{\{K\}}\right)^{-1} \tag{2.13}$$

Figure 2.5 presents the dynamics of the plant when decoupled using the Jacobian matrix expressed at the center of stiffness. The plant is well decoupled below the suspension mode with the lowest frequency (2.14), making it particularly suitable for systems with high stiffness.

$$\boldsymbol{G}_{\{K\}}(j\omega) \xrightarrow[\omega\to 0]{} \boldsymbol{J}_{\{K\}}^{-1}\boldsymbol{\mathcal{K}}^{-1}\boldsymbol{J}_{\{K\}}^{-\intercal} \tag{2.14}$$

The physical reason for high-frequency coupling is illustrated in Figure 2.5b. When a high-frequency force is applied at a point not aligned with the center of mass, it induces rotation around the center of mass. This phenomenon explains the coupling observed between different degrees of freedom at higher frequencies.

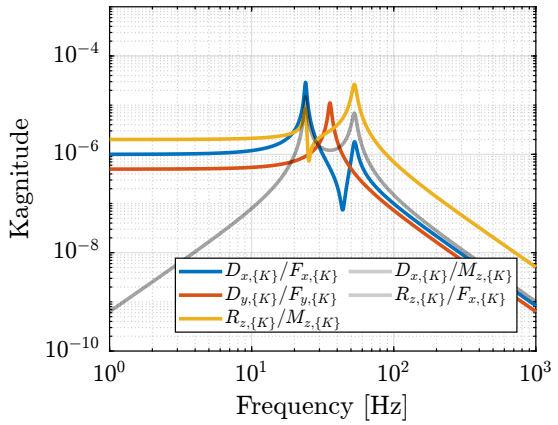

(a) Dynamics at the CoK

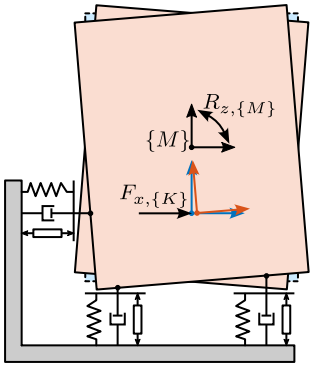

(b) High frequency force applied at the CoK

Figure 2.5: Plant decoupled using the Jacobian matrix expresssed at the center of stiffness (a). The physical reason for high frequency coupling is illustrated in (b).

2.4 Modal Decoupling

Modal decoupling represents an approach based on the principle that a mechanical system's behavior can be understood as a combination of contributions from various modes [47].

To convert the dynamics in the modal space, the equation of motion are first written with respect to the center of mass (2.15).

$$\boldsymbol{M}_{\{M\}}\ddot{\boldsymbol{\mathcal{X}}}_{\{M\}}(t) + \boldsymbol{C}_{\{M\}}\dot{\boldsymbol{\mathcal{X}}}_{\{M\}}(t) + \boldsymbol{K}_{\{M\}}\boldsymbol{\mathcal{X}}_{\{M\}}(t) = \boldsymbol{J}_{\{M\}}^{\intercal}\boldsymbol{\tau}(t) \tag{2.15}$$

For modal decoupling, a change of variables is introduced (2.16) where $\boldsymbol{\mathcal{X}}_m$ represents the modal amplitudes and $\boldsymbol{\Phi}$ is a $n \times n$[1] matrix whose columns correspond to the mode shapes of the system, computed from $\boldsymbol{M}_{\{M\}}$ and $\boldsymbol{K}_{\{M\}}$.

$$\boldsymbol{\mathcal{X}}_{\{M\}} = \boldsymbol{\Phi}\boldsymbol{\mathcal{X}}_m \tag{2.16}$$

By pre-multiplying equation (2.15) by $\boldsymbol{\Phi}^{\intercal}$ and applying the change of variable (2.16), a new set of equations of motion is obtained (2.17) where $\boldsymbol{\tau}_m$ represents the modal input, while $\boldsymbol{M}_m$, $\boldsymbol{C}_m$, and $\boldsymbol{K}_m$ denote the modal mass, damping, and stiffness matrices respectively.

$$\underbrace{\boldsymbol{\Phi}^{\intercal}\boldsymbol{M}\boldsymbol{\Phi}}_{\boldsymbol{M}_m}\ddot{\boldsymbol{\mathcal{X}}}_m(t) + \underbrace{\boldsymbol{\Phi}^{\intercal}\boldsymbol{C}\boldsymbol{\Phi}}_{\boldsymbol{C}_m}\dot{\boldsymbol{\mathcal{X}}}_m(t) + \underbrace{\boldsymbol{\Phi}^{\intercal}\boldsymbol{K}\boldsymbol{\Phi}}_{\boldsymbol{K}_m}\boldsymbol{\mathcal{X}}_m(t) = \underbrace{\boldsymbol{\Phi}^{\intercal}\boldsymbol{J}^{\intercal}\boldsymbol{\tau}(t)}_{\boldsymbol{\tau}_m(t)} \tag{2.17}$$

The inherent mathematical structure of the mass, damping, and stiffness matrices [48, chapt. 8] ensures that modal matrices are diagonal [49, chapt. 2.3]. This diagonalization transforms equation (2.17) into a set of n decoupled equations, enabling independent control of each mode without cross-interaction.

To implement this approach from a decentralized plant, the architecture shown in Figure 2.6 is employed. Inputs of the decoupling plant are the modal modal inputs $\boldsymbol{\tau}_m$ and the outputs are the modal amplitudes $\boldsymbol{\mathcal{X}}_m$. This implementation requires knowledge of the system's equations of motion, from which the mode shapes matrix $\boldsymbol{\Phi}$ is derived. The resulting decoupled system features diagonal elements each representing second-order resonant systems that are straightforward to control individually.

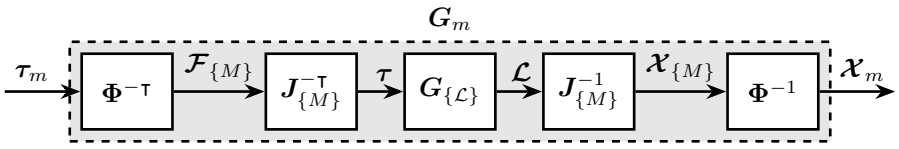

Figure 2.6: Modal Decoupling Architecture

Modal decoupling was then applied to the test model. First, the eigenvectors $\boldsymbol{\Phi}$ of $\boldsymbol{M}_{\{M\}}^{-1}\boldsymbol{K}_{\{M\}}$ were computed (2.18). While analytical derivation of eigenvectors could be obtained for such a simple system, they are typically computed numerically for practical applications.

$$\boldsymbol{\Phi} = \begin{bmatrix} \frac{I - h_a^2 m - 2l_a^2 m - \alpha}{2h_a m} & 0 & \frac{I - h_a^2 m - 2l_a^2 m + \alpha}{2h_a m} \\ 0 & 1 & 0 \\ 1 & 0 & 1 \end{bmatrix}, \quad \alpha = \sqrt{\left(I + m(h_a^2 - 2l_a^2)\right)^2 + 8m^2 h_a^2 l_a^2} \tag{2.18}$$

The numerical values for the eigenvector matrix and its inverse are shown in (2.19).

$$\boldsymbol{\Phi} = \begin{bmatrix} -0.905 & 0 & -0.058 \\ 0 & 1 & 0 \\ 0.424 & 0 & -0.998 \end{bmatrix}, \quad \boldsymbol{\Phi}^{-1} = \begin{bmatrix} -1.075 & 0 & 0.063 \\ 0 & 1 & 0 \\ -0.457 & 0 & -0.975 \end{bmatrix} \tag{2.19}$$

[1] n corresponds to the number of degrees of freedom, here $n = 3$

The two computed matrices were implemented in the control architecture of Figure 2.6, resulting in three distinct second order plants as depicted in Figure 2.7a. Each of these diagonal elements corresponds to a specific mode, as shown in Figure 2.7b, resulting in a perfectly decoupled system.

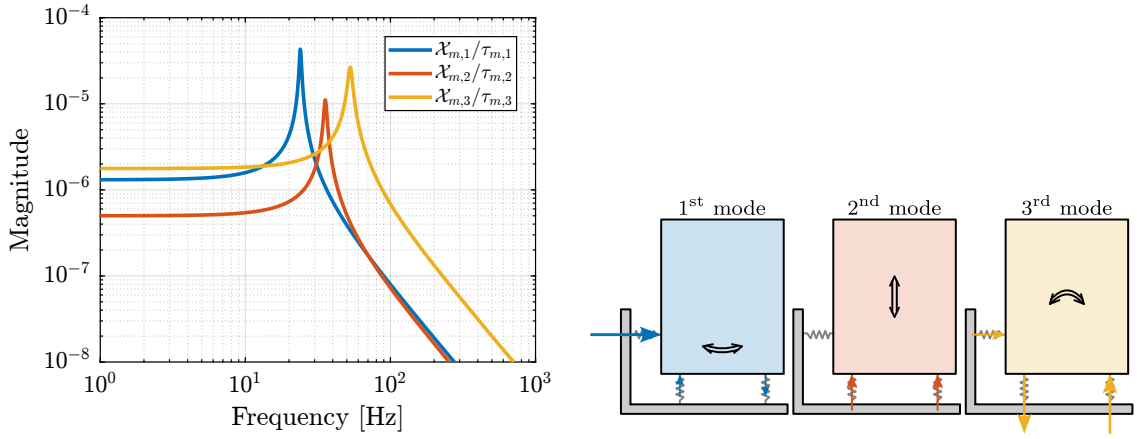

(a) Decoupled plant in modal space

(b) Individually controlled modes

Figure 2.7: Plant using modal decoupling consists of second order plants (a) which can be used to invidiually address different modes illustrated in (b)

2.5 SVD Decoupling

Singular Value Decomposition Singular Value Decomposition (SVD) represents a powerful mathematical tool with extensive applications in data analysis [50, chapt. 1] and multivariable control systems [36], where it is particularly valuable for analyzing directional properties in multivariable systems.

The SVD constitutes a unique matrix decomposition applicable to any complex matrix $\boldsymbol{X} \in \mathbb{C}^{n\times m}$, expressed as:

$$\boldsymbol{X} = \boldsymbol{U}\boldsymbol{\Sigma}\boldsymbol{V}^H \tag{2.20}$$

where $\boldsymbol{U} \in \mathbb{C}^{n\times n}$ and $\boldsymbol{V} \in \mathbb{C}^{m\times m}$ are unitary matrices with orthonormal columns, and $\boldsymbol{\Sigma} \in \mathbb{R}^{n\times n}$ is a diagonal matrix with real, non-negative entries. For real matrices $\boldsymbol{X}$, the resulting $\boldsymbol{U}$ and $\boldsymbol{V}$ matrices are also real, making them suitable for decoupling applications.

Decoupling using the SVD The procedure for SVD-based decoupling begins with identifying the system dynamics from inputs to outputs, typically represented as a Frequency Response Function (FRF), which yields a complex matrix $\boldsymbol{G}(\omega_i)$ for multiple frequency points ω_i. A specific frequency is then selected for optimal decoupling, with the targeted crossover frequency ω_c often serving as an appropriate choice.

Since real matrices are required for the decoupling transformation, a real approximation of the complex measured response at the selected frequency must be computed. In this work, the method proposed in

[51] was used as it preserves maximal orthogonality in the directional properties of the input complex matrix.

Following this approximation, a real matrix $\tilde{\boldsymbol{G}}(\omega_c)$ is obtained, and SVD is performed on this matrix. The resulting (real) unitary matrices $\boldsymbol{U}$ and $\boldsymbol{V}$ are structured such that $\boldsymbol{V}^{-\intercal}\tilde{\boldsymbol{G}}(\omega_c)\boldsymbol{U}^{-1}$ forms a diagonal matrix. These singular input and output matrices are then applied to decouple the system as illustrated in Figure 2.8, and the decoupled plant is described by (2.21).

$$\boldsymbol{G}_{\text{SVD}}(s) = \boldsymbol{U}^{-1}\boldsymbol{G}_{\{\mathcal{L}\}}(s)\boldsymbol{V}^{-\intercal} \tag{2.21}$$

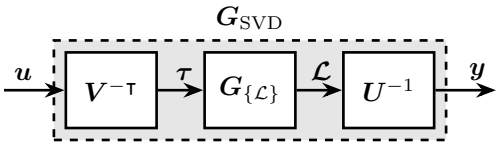

Figure 2.8: Decoupled plant $\boldsymbol{G}_{\text{SVD}}$ using the Singular Value Decomposition

Implementation of SVD decoupling requires access to the system's FRF, at least in the vicinity of the desired decoupling frequency. This information can be obtained either experimentally or derived from a model. While this approach ensures effective decoupling near the chosen frequency, it provides no guarantees regarding decoupling performance away from this frequency. Furthermore, the quality of decoupling depends significantly on the accuracy of the real approximation, potentially limiting its effectiveness for plants with high damping.

Example Plant decoupling using the Singular Value Decomposition was then applied on the test model. A decoupling frequency of 100 Hz was used. The plant response at that frequency, as well as its real approximation and the obtained $\boldsymbol{U}$ and $\boldsymbol{V}$ matrices are shown in (2.22).

$$\begin{aligned}
\boldsymbol{G}_{\{\mathcal{L}\}}(\omega_c = 2\pi\cdot 100) &= 10^{-9}\begin{bmatrix} -99-j2.6 & 74+j4.2 & -74-j4.2 \\ 74+j4.2 & -247-j9.7 & 102+j7.0 \\ -74-j4.2 & 102+j7.0 & -247-j9.7 \end{bmatrix} \\
&\xrightarrow[\text{approximation}]{\text{real}} \tilde{\boldsymbol{G}}_{\{\mathcal{L}\}}(\omega_c) = 10^{-9}\begin{bmatrix} -99 & 74 & -74 \\ 74 & -247 & 102 \\ -74 & 102 & -247 \end{bmatrix} \\
&\xrightarrow[\text{SVD}]{} \boldsymbol{U} = \begin{bmatrix} 0.34 & 0 & 0.94 \\ -0.66 & 0.71 & 0.24 \\ 0.66 & 0.71 & -0.24 \end{bmatrix},\ \boldsymbol{V} = \begin{bmatrix} -0.34 & 0 & -0.94 \\ 0.66 & -0.71 & -0.24 \\ -0.66 & -0.71 & 0.24 \end{bmatrix}
\end{aligned} \tag{2.22}$$

Using these $\boldsymbol{U}$ and $\boldsymbol{V}$ matrices, the decoupled plant is computed according to equation (2.21). The resulting plant, depicted in Figure 2.9, exhibits remarkable decoupling across a broad frequency range, extending well beyond the vicinity of ω_c. Additionally, the diagonal terms manifest as second-order dynamic systems, facilitating straightforward controller design.

As it was surprising to obtain such a good decoupling at all frequencies, a variant system with identical dynamics but different sensor configurations was examined. Instead of using relative motion sensors aligned with the struts, three relative motion sensors were positioned as shown in Figure 2.10a. Although Jacobian matrices could theoretically map between these different sensor arrangements, application of the same SVD decoupling procedure yielded the plant response shown in Figure 2.10b, which exhibits

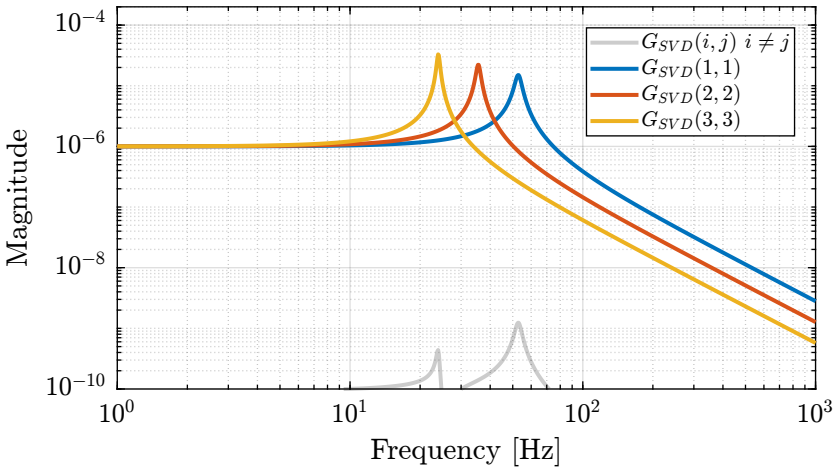

Figure 2.9: Plant dynamics $\boldsymbol{G}_{\text{SVD}}(s)$ obtained after decoupling using Singular Value Decomposition

significantly greater coupling. Notably, the coupling demonstrates local minima near the decoupling frequency, consistent with the fact that the decoupling matrices were derived specifically for that frequency point.

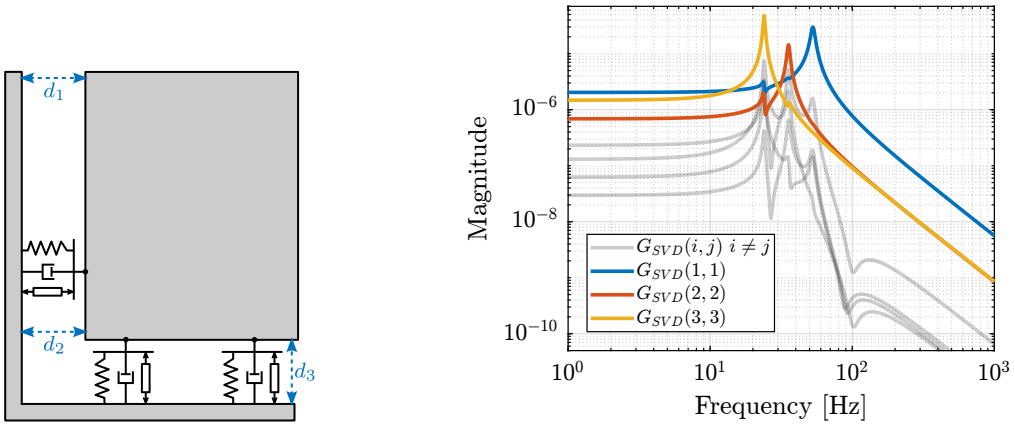

(a) Alternative location of sensors

(b) Obtained decoupled plant

Figure 2.10: Application of SVD decoupling on a system schematically shown in (a). The obtained decoupled plant is shown in (b).

The exceptional performance of SVD decoupling on the plant with collocated sensors warrants further investigation. This effectiveness may be attributed to the symmetrical properties of the plant, as evidenced in the Bode plots of the decentralized plant shown in Figure 2.2. The phenomenon potentially relates to previous research on SVD controllers applied to systems with specific symmetrical characteristics [52].

2.6 Comparison of decoupling strategies

While the three proposed decoupling methods may appear similar in their mathematical implementation (each involving pre-multiplication and post-multiplication of the plant with constant matrices), they differ significantly in their underlying approaches and practical implications, as summarized in Table 2.2.

Each method employs a distinct conceptual framework: Jacobian decoupling is "topology-driven", relying on the geometric configuration of the system; modal decoupling is "physics-driven", based on the system's dynamical equations; and SVD decoupling is "data-driven", utilizing measured frequency response functions.

The physical interpretation of decoupled plant inputs and outputs varies considerably among these methods. With Jacobian decoupling, inputs and outputs retain clear physical meaning, corresponding to forces/torques and translations/rotations in a specified reference frame. Modal decoupling arranges inputs to excite individual modes, with outputs combined to measure these modes separately. For SVD decoupling, inputs and outputs represent special directions ordered by decreasing controllability and observability at the chosen frequency, though physical interpretation becomes challenging for parallel manipulators.

This difference in interpretation relates directly to the "control space" in which the controllers operate. When these "control spaces" meaningfully relate to the control objectives, controllers can be tuned to directly match specific requirements. For Jacobian decoupling, the controller typically operates in a frame positioned at the point where motion needs to be controlled, for instance where the light is focused in the NASS application. Modal decoupling provides a natural framework when specific vibrational modes require targeted control. SVD decoupling generally results in a loss of physical meaning for the "control space", potentially complicating the process of relating controller design to practical system requirements.

The quality of decoupling achieved through these methods also exhibits distinct characteristics. Jacobian decoupling performance depends on the chosen reference frame, with optimal decoupling at low frequencies when aligned at the center of stiffness, or at high frequencies when aligned with the center of mass. Systems designed with coincident centers of mass and stiffness may achieve excellent decoupling using this approach. Modal decoupling offers good decoupling across all frequencies, though its effectiveness relies on the accuracy of the system model, with discrepancies potentially resulting in significant off-diagonal elements. The diagonal elements typically manifest as second-order low-pass filters, facilitating straightforward control design. SVD decoupling can be implemented using measured data without requiring a model, with optimal performance near the chosen decoupling frequency, though its effectiveness may diminish at other frequencies and depends on the quality of the real approximation of the response at the selected frequency point.

Table 2.2: Comparison of decoupling strategies

	Jacobian	**Modal**	**SVD**
Philosophy	Topology Driven	Physics Driven	Data Driven
Requirements	Known geometry	Known equations of motion	Identified FRF
Decoupling Matrices	Decoupling using $\boldsymbol{J}_{\{O\}}$ obtained from geometry	Decoupling using $\boldsymbol{\Phi}$ obtained from modal decomposition	Decoupling using $\boldsymbol{U}$ and $\boldsymbol{V}$ obtained from SVD
Decoupled Plant	$\boldsymbol{G}_{\{O\}}(s) = \boldsymbol{J}_{\{O\}}^{-1}\boldsymbol{G}_{\mathcal{L}}(s)\boldsymbol{J}_{\{O\}}^{-\intercal}$	$\boldsymbol{G}_m(s) = \boldsymbol{\Phi}^{-1}\boldsymbol{G}_{\mathcal{X}}(s)\boldsymbol{\Phi}^{-\intercal}$	$\boldsymbol{G}_{\text{SVD}}(s) = \boldsymbol{U}^{-1}\boldsymbol{G}(s)\boldsymbol{V}^{-\intercal}$
Controller	$\boldsymbol{K}_{\{O\}}(s) = \boldsymbol{J}_{\{O\}}^{-\intercal}\boldsymbol{K}_d(s)\boldsymbol{J}_{\{O\}}^{-1}$	$\boldsymbol{K}_m(s) = \boldsymbol{\Phi}^{-\intercal}\boldsymbol{K}_d(s)\boldsymbol{\Phi}^{-1}$	$\boldsymbol{K}_{\text{SVD}}(s) = \boldsymbol{V}^{-\intercal}\boldsymbol{K}_d(s)\boldsymbol{U}^{-1}$
Interpretation	Forces/Torques to Displacement/Rotation in chosen frame	Inputs to excite individual modes Output to sense individual modes	Directions of max to min controllability/observability
Properties	Decoupling at low or high frequency depending on the chosen frame	Good decoupling at all frequencies	Good decoupling near the chosen frequency
Pros	Physical inputs / outputs Good decoupling at High frequency (diagonal mass matrix if Jacobian taken at the CoM) Good decoupling at Low frequency (if Jacobian taken at specific point) Easy integration of meaningful reference inputs	Target specific modes 2nd order diagonal plant	Good Decoupling near the crossover Very General
Cons	Coupling between force/rotation may be high at low frequency (non diagonal terms in K) Limited to parallel mechanisms (?) If good decoupling at all frequencies =¿ requires specific mechanical architecture	Need analytical equations	Loose the physical meaning of inputs /outputs Decoupling depends on the real approximation validity Diagonal plants may not be easy to control
Applicability	Parallel Mechanisms Only small motion for the Jacobian matrix to stay constant	Systems whose dynamics that can be expressed with M and K matrices	Very general Need FRF data (either experimentally or analytically)

3 Closed-Loop Shaping using Complementary Filters

Once the system is properly decoupled using one of the approaches described in Section 2, SISO controllers can be individually tuned for each decoupled "directions". Several ways to design a controller to obtain a given performance while ensuring good robustness properties can be implemented.

In some cases, "fixed" controller structures are utilized, such as PI and PID controllers [9], [37], [38]. In such cases, the controller coefficients are manually tuned to obtain acceptable performance and robustness.

Another popular method is Open-Loop shaping, that was used during the conceptual phase after the plan was decoupled in the frame of the struts. The idea of open-loop shaping is to tune the controller (using a series of standard leads, lags, notches, low pass filters) such that the open-loop transfer function $G(s)K(s)$ is made according to specification (i.e. bandwidth, gain and phase margins, gain at a specific frequency, etc...) [53, chapt. 4.4.7]. Open-Loop shaping is very popular because the open-loop transfer function depends linearly on the controller, making it relatively straightforward to tune the controller to achieve desired open-loop characteristics. Another key advantage is that controllers can be tuned directly from measured frequency response functions without requiring an explicit plant model.

However, the behavior (i.e. performance) of a feedback system is a function of closed-loop transfer functions [36, chapt. 3]. Specifications can therefore be expressed in terms of the magnitude of closed-loop transfer functions, such as the sensitivity, plant sensitivity, and complementary sensitivity transfer functions. With open-loop shaping, closed-loop transfer functions are changed only indirectly, which may make it difficult to directly address the specifications that are in terms of the closed-loop transfer functions.

In order to synthesize a controller that directly shapes the closed-loop transfer functions (and therefore the performance metric), $\mathcal{H}_\infty$ loop-shaping may be used [36]. This approach requires a good model of the plant and expertise in selecting weighting functions that will define the wanted shape of different closed-loop transfer functions [54]. $\mathcal{H}_\infty$ synthesis has been applied for the Stewart platform [45], but comparative studies with more simple decentralized controllers did not show large improvements [5], [8].

In this section, an alternative controller synthesis scheme is proposed in which complementary filters are used for directly shaping the closed-loop transfer functions (i.e., directly addressing the closed-loop performances).

In Section 3.1, the proposed control architecture including the complementary filters is presented. In Section 3.2, typical performance requirements are translated into the shape of the complementary filters. The design of the complementary filters is briefly discussed in Section 3.3, and analytical formulas are proposed such that it is possible to change the closed-loop behavior of the system in real time. Finally, in Section 3.4, a numerical example is used to show how the proposed control architecture can be implemented in practice.

3.1 Control Architecture

Virtual Sensor Fusion The concept of using complementary filters in control architecture originates from sensor fusion techniques [18], where two sensors are combined using complementary filters. Building upon this concept, "virtual sensor fusion" [55] replaces one physical sensor with a model G of the plant.

The control architecture is illustrated in Figure 3.1a, where G' represents the physical plant to be controlled, G is a model of the plant, k is the controller, and H_L and H_H are complementary filters satisfying $H_L(s) + H_H(s) = 1$. In this arrangement, the physical plant is controlled at low frequencies, while the plant model is utilized at high frequencies to enhance robustness.

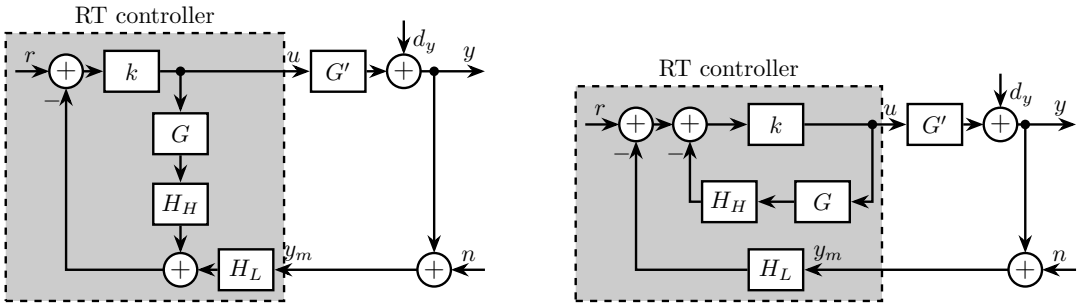

(a) Virtual Sensor Fusion **(b)** Equivalent Architecture

Figure 3.1: Control architecture for virtual sensor fusion (a). An equivalent architecture is shown in (b). The signals are the reference signal r, the output perturbation d_y, the measurement noise n and the control input u.

Although the control architecture shown in Figure 3.1a appears to be a multi-loop system, it should be noted that no non-linear saturation-type elements are present in the inner loop (containing k, G, and H_H, all numerically implemented). Consequently, this structure is mathematically equivalent to the single-loop architecture illustrated in Figure 3.1b.

Asymptotic behavior When considering the extreme case of very high values for k, the effective controller $K(s)$ converges to the inverse of the plant model multiplied by the inverse of the high-pass filter, as expressed in (3.1).

$$\lim_{k\to\infty} K(s) = \lim_{k\to\infty} \frac{k}{1 + H_H(s)G(s)k} = (H_H(s)G(s))^{-1} \tag{3.1}$$

If the resulting K is improper, a low-pass filter with sufficiently high corner frequency can be added to ensure its causal realization. Furthermore, for K to be stable, both G and H_H must be minimum phase transfer functions.

With these assumptions, the resulting control architecture is illustrated in Figure 3.2, where the complementary filters H_L and H_H remain the only tuning parameters. The dynamics of this closed-loop system are described by (3.2).

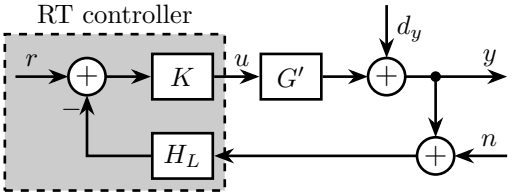

Figure 3.2: Equivalent classical feedback control architecture

$$y = \frac{H_H dy + G'G^{-1}r - G'G^{-1}H_L n}{H_H + G'G^{-1}H_L} \tag{3.2a}$$

$$u = \frac{-G^{-1}H_L dy + G^{-1}r - G^{-1}H_L n}{H_H + G'G^{-1}H_L} \tag{3.2b}$$

At frequencies where the model accurately represents the physical plant ($G^{-1}G' \approx 1$), the denominator simplifies to $H_H + G'G^{-1}H_L \approx H_H + H_L = 1$, and the closed-loop transfer functions are described by (3.3).

$$y = H_H dy \quad + r \quad - H_L n \tag{3.3a}$$

$$u = -G^{-1}H_L dy + G^{-1}r - G^{-1}H_L n \tag{3.3b}$$

The sensitivity transfer function equals the high-pass filter $S = \frac{y}{dy} = H_H$, and the complementary sensitivity transfer function equals the low-pass filter $T = \frac{y}{n} = H_L$. Hence, when the plant model closely approximates the actual system, the closed-loop behavior becomes fully determined by the designed complementary filters, enabling direct translation of performance requirements into filter design.

3.2 Translating the performance requirements into the shapes of the complementary filters

Performance specifications in feedback systems can be expressed as upper bounds on the magnitudes of closed-loop transfer functions such that the sensitivity $|S(j\omega)|$ and complementary sensitivity $|T(j\omega)|$ transfer functions [54]. The design of a controller $K(s)$ to achieve desired shapes of these closed-loop transfer functions is known as closed-loop shaping.

In the proposed control architecture, the closed-loop transfer functions (3.2) are expressed in terms of the complementary filters $H_L(s)$ and $H_H(s)$ rather than directly through the controller $K(s)$. Therefore, performance requirements must be translated into constraints on the shapes of these complementary filters.

Nominal Stability (NS) A closed-loop system is stable when all its elements (here K, G', and H_L) are stable and the sensitivity function $S = \frac{1}{1+G'KH_L}$ is stable. For the nominal system ($G' = G$), the sensitivity transfer function equals the high-pass filter: $S(s) = H_H(s)$.

Nominal stability is therefore guaranteed when H_L, H_H, and G are stable, and both G and H_H are minimum phase (ensuring K is stable). Consequently, stable and minimum phase complementary filters must be employed.

Nominal Performance (NP) Performance specifications can be formalized using weighting functions w_H and w_L, where performance is achieved when (3.4) is satisfied.

$$|w_H(j\omega)S(j\omega)| \leq 1 \quad \forall\omega \tag{3.4a}$$
$$|w_L(j\omega)T(j\omega)| \leq 1 \quad \forall\omega \tag{3.4b}$$

For the nominal system, where $S = H_H$ and $T = H_L$, nominal performance is ensured by satisfying (3.5).

$$\boxed{\text{NP} \iff \begin{cases} |w_H(j\omega)H_H(j\omega)| \leq 1 & \forall\omega \\ |w_L(j\omega)H_L(j\omega)| \leq 1 & \forall\omega \end{cases}} \tag{3.5}$$

Typical performance requirements can therefore be translated into constraints on the complementary filters. For disturbance rejection, the magnitude of the sensitivity function $|S(j\omega)| = |H_H(j\omega)|$ should be minimized, particularly at low frequencies where disturbances are usually most prominent. Similarly, for noise attenuation, the magnitude of the complementary sensitivity function $|T(j\omega)| = |H_L(j\omega)|$ should be minimized, especially at high frequencies where measurement noise typically dominates. The closed-loop bandwidth can be effectively limited by ensuring that $|T(j\omega)|$ remains below $\frac{1}{\sqrt{2}}$ at frequencies above the maximum desired bandwidth. By carefully selecting the shapes of these complementary filters, nominal performance specifications can be directly addressed in an intuitive manner.

Classical stability margins (gain and phase margins) are also related to the maximum amplitude of the sensitivity transfer function. Typically, maintaining $|S|_\infty \leq 2$ ensures a gain margin of at least 2 and a phase margin of at least 29°.

Robust Stability (RS) Robust stability refers to a control system's ability to maintain stability despite discrepancies between the actual system G' and the model G used for controller design. These discrepancies may arise from unmodeled dynamics or nonlinearities.

To represent these model-plant differences, input multiplicative uncertainty as illustrated in Figure 3.3a is employed. The set of possible plants Π_i is described by (3.6). With the weighting function w_I selected such that all possible plants G' are contained within the set Π_i.

$$\Pi_i: \quad G'(s) = G(s)\big(1 + w_I(s)\Delta_I(s)\big); \quad |\Delta_I(j\omega)| \leq 1 \ \forall\omega \tag{3.6}$$

When considering input multiplicative uncertainty, robust stability can be derived graphically from the Nyquist plot (illustrated in Figure 3.3b), yielding to (3.7), as demonstrated in [36, chapt. 7.5.1].

$$\text{RS} \iff |w_I(j\omega)L(j\omega)| \leq |1 + L(j\omega)| \quad \forall\omega \tag{3.7}$$

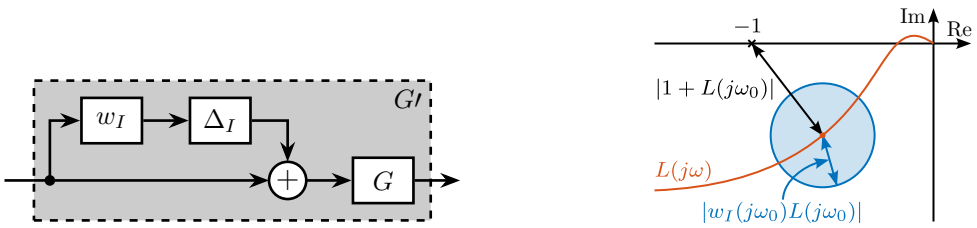

(a) Input multiplicative uncertainty **(b)** Nyquist plot - Effect of multiplicative uncertainty

Figure 3.3: Input multiplicative uncertainty to model the differences between the model and the physical plant (a). Effect of this uncertainty is displayed on the Nyquist plot (b)

After algebraic manipulation, robust stability is guaranteed when the low-pass complementary filter H_L satisfies (3.8).

$$\boxed{\text{RS} \iff |w_I(j\omega)H_L(j\omega)| \leq 1 \quad \forall\omega} \tag{3.8}$$

Robust Performance (RP) Robust performance ensures that performance specifications (3.4) are met even as plant dynamics varies within specified bounds. This requires the performance condition to be valid for all possible plants in the defined uncertainty set Π_i:

$$\text{RP} \iff |w_H(j\omega)S(j\omega)| \leq 1 \quad \forall G' \in \Pi_I,\ \forall\omega \tag{3.9}$$

Transforming this condition into constraints on the complementary filters yields:

$$\boxed{\text{RP} \iff |w_H(j\omega)H_H(j\omega)| + |w_I(j\omega)H_L(j\omega)| \leq 1,\ \forall\omega} \tag{3.10}$$

The robust performance condition effectively combines both nominal performance (3.5) and robust stability conditions (3.8). If both NP and RS conditions are satisfied, robust performance will be achieved within a factor of 2 [36, chapt. 7.6]. Therefore, for SISO systems, ensuring robust stability and nominal performance is typically sufficient.

3.3 Complementary filter design

As proposed in Section 1, complementary filters can be shaped using standard $\mathcal{H}_\infty$ synthesis techniques. This approach is particularly well-suited since performance requirements were expressed as upper bounds on the magnitude of the complementary filters (Section 3.2).

Alternatively, analytical formulas for complementary filters may be employed. For some applications, first-order complementary filters as shown in Equation (3.11) are sufficient.

$$H_L(s) = \frac{1}{1 + s/\omega_0} \tag{3.11a}$$

$$H_H(s) = \frac{s/\omega_0}{1 + s/\omega_0} \tag{3.11b}$$

These filters can be transformed into the digital domain using the Bilinear transformation, resulting in the digital filter representations shown in Equation (3.12).

$$H_L(z^{-1}) = \frac{T_s\omega_0 + T_s\omega_0 z^{-1}}{T_s\omega_0 + 2 + (T_s\omega_0 - 2)z^{-1}} \tag{3.12a}$$

$$H_H(z^{-1}) = \frac{2 - 2z^{-1}}{T_s\omega_0 + 2 + (T_s\omega_0 - 2)z^{-1}} \tag{3.12b}$$

A significant advantage of using analytical formulas for complementary filters is that key parameters such as ω_0 can be modified in real-time, as illustrated in Figure 3.4. This real-time tunability allows rapid testing of different control bandwidths to evaluate performance and robustness characteristics.

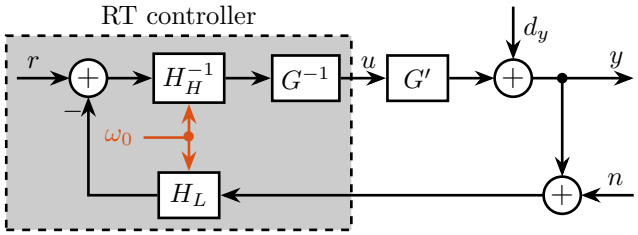

Figure 3.4: Implemented digital complementary filters with parameter ω_0 that can be changed in real time

For many practical applications, first order complementary filters are not sufficient. Specifically, a slope of $+2$ at low frequencies for the sensitivity transfer function (enabling accurate tracking of ramp inputs) and a slope of -2 for the complementary sensitivity transfer function are often desired. For these cases, the second-order complementary filters presented in Equation (3.13) are proposed.

$$H_L(s) = \frac{(1+\alpha)(\frac{s}{\omega_0}) + 1}{\left((\frac{s}{\omega_0}) + 1\right)\left((\frac{s}{\omega_0})^2 + \alpha(\frac{s}{\omega_0}) + 1\right)} \tag{3.13a}$$

$$H_H(s) = \frac{(\frac{s}{\omega_0})^2\left((\frac{s}{\omega_0}) + 1 + \alpha\right)}{\left((\frac{s}{\omega_0}) + 1\right)\left((\frac{s}{\omega_0})^2 + \alpha(\frac{s}{\omega_0}) + 1\right)} \tag{3.13b}$$

The influence of parameters α and ω_0 on the frequency response of these complementary filters is illustrated in Figure 3.5. The parameter α primarily affects the damping characteristics near the crossover frequency, while ω_0 determines the frequency at which the transition between high-pass and low-pass behavior occurs. These filters can also be implemented in the digital domain with analytical formulas, preserving the ability to adjust α and ω_0 in real-time.

The presented analytical formulations offer an attractive balance between design simplicity and performance. This capability to tune parameters in real-time is particularly valuable during commissioning of the controller.

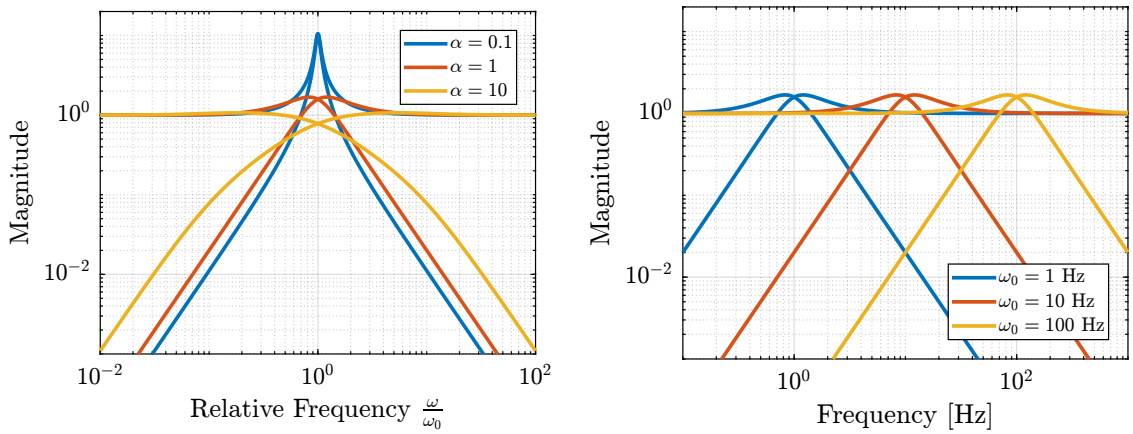

(a) Effect of α

(b) Effect of ω_0

Figure 3.5: Shape of proposed analytical complementary filters. Effect of α (a) and ω_0 (b) are shown.

3.4 Numerical Example

To systematically apply the proposed control technique, the following procedure is recommended:

1. Identify the plant to be controlled to obtain the plant model G.
2. Design the weighting function w_I such that all possible plants G' are contained in the uncertainty set Π_i.
3. Translate performance requirements into upper bounds on the complementary filters as explained in Section 3.2.
4. Design the weighting functions w_H and w_L and generate the complementary filters using $\mathcal{H}_\infty$-synthesis as described in Section 1.3. If the synthesis fails to produce filters satisfying the defined upper bounds, either revise the requirements or develop a more accurate model G that will allow for a smaller w_I. For simpler cases, the analytical formulas for complementary filters presented in Section 3.3 can be employed.
5. If $K(s) = H_H^{-1}(s)G^{-1}(s)$ is not proper, add low-pass filters with sufficiently high corner frequencies to ensure realizability.

Plant To evaluate this control architecture, a simple test model representative of many synchrotron positioning stages is utilized (Figure 3.6a). In this model, a payload with mass m is positioned on top of a stage. The objective is to accurately position the sample relative to the X-ray beam.

The relative position y between the payload and the X-ray is measured, which typically involves measuring the relative position between the focusing optics and the sample. Various disturbance forces

affect positioning stability, including stage vibrations d_w and direct forces applied to the sample d_F (such as cable forces). The positioning stage itself is characterized by stiffness k, internal damping c, and a controllable force F.

The model of the plant $G(s)$ from actuator force F to displacement y is described by Equation (3.14).

$$G(s) = \frac{1}{ms^2 + cs + k} \tag{3.14}$$

The parameter values are set to $m = 20\,\text{kg}$, $k = 1\text{N}/\mu\text{m}$, and $c = 10^2\text{N}/(\text{m/s})$.

The plant dynamics include uncertainties related to limited support compliance, unmodeled flexible dynamics, payload dynamics, and other factors. These uncertainties are represented using a multiplicative input uncertainty weight (3.15)., which specifies the magnitude of uncertainty as a function of frequency:

$$w_I(s) = 10 \cdot \frac{(s+100)^2}{(s+1000)^2} \tag{3.15}$$

Figure 3.6b illustrates both the nominal plant dynamics and the complete set of possible plants Π_i encompassed by the uncertainty model.

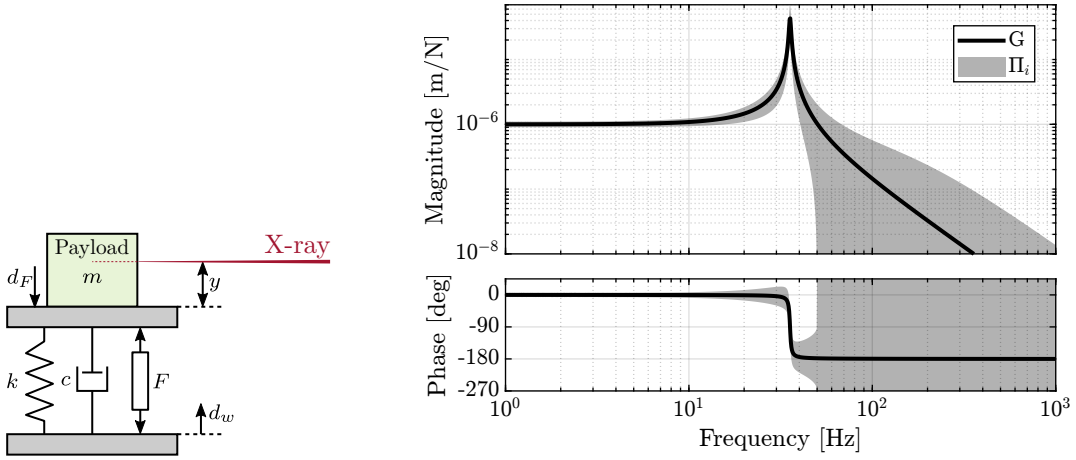

(a) Test model

(b) Bode plot of $G(s)$ and associated uncertainty set

Figure 3.6: Schematic of the test system (a). Bode plot of the transfer function $G(s)$ from F to y and the associated uncertainty set (b).

Requirements and choice of complementary filters As discussed in Section 3.2, nominal performance requirements can be expressed as upper bounds on the shapes of the complementary filters. For this example, the requirements are:

- to track ramp inputs (constant velocity scans) with zero steady-state error, which necessitates a +2 slope at low frequencies for the magnitude of the sensitivity function $|S(j\omega)|$

- filtering of measurement noise above 300 Hz, where sensor noise is significant (requiring a filtering factor of approximately 100 above this frequency)

- maximizing disturbance rejection

Additionally, robust stability must be ensured, requiring the closed-loop system to remain stable despite the dynamic uncertainties modeled by w_I. This condition is satisfied when the magnitude of the low-pass complementary filter $|H_L(j\omega)|$ remains below the inverse of the uncertainty weight magnitude $|w_I(j\omega)|$, as expressed in Equation (3.8).

Robust performance is achieved when both nominal performance and robust stability conditions are simultaneously satisfied.

All requirements imposed on H_L and H_H are visualized in Figure 3.7a. While $\mathcal{H}_\infty$ synthesis could be employed to design the complementary filters, analytical formulas were used for this relatively simple example. Specifically, the second-order complementary filters from Equation (3.13) were selected, providing the desired $+2$ and -2 slopes, with parameters $\alpha = 1$ and $\omega_0 = 2\pi \cdot 20$ Hz.

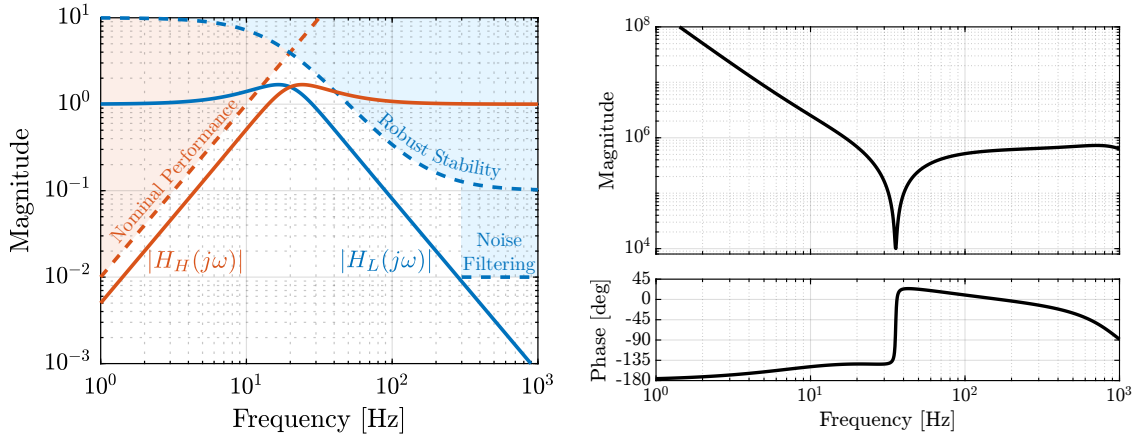

(a) Specifications and complementary filters

(b) Bode plot of $K(s) \cdot H_L(s)$

Figure 3.7: Performance requirement and complementary filters used (a). Obtained controller from the complementary filters and the plant inverse is shown in (b).

Controller analysis The controller to be implemented takes the form $K(s) = \tilde{G}^{-1}(s)H_H^{-1}(s)$, where $\tilde{G}^{-1}(s)$ represents the plant inverse, which must be both stable and proper. To ensure properness, low-pass filters with high corner frequencies are added as shown in Equation (3.16).

$$\tilde{G}^{-1}(s) = \frac{ms^2 + cs + k}{1 + \frac{s}{2\pi \cdot 1000} + \left(\frac{s}{2\pi \cdot 1000}\right)^2} \tag{3.16}$$

The Bode plot of the controller multiplied by the complementary low-pass filter, $K(s) \cdot H_L(s)$, is presented in Figure 3.7b. The frequency response reveals several important characteristics:

- The presence of two integrators at low frequencies, enabling accurate tracking of ramp inputs

- A notch at the plant resonance frequency (arising from the plant inverse)

- A lead component near the control bandwidth of approximately 20 Hz, enhancing stability margins

Robustness and Performance analysis Robust stability is assessed using the Nyquist plot shown in Figure 3.8a. Even when considering all possible plants within the uncertainty set, the Nyquist plot remains sufficiently distant from the critical point $(-1, 0)$, indicating robust stability with adequate margins.

Performance is evaluated by examining the closed-loop sensitivity and complementary sensitivity transfer functions, as illustrated in Figure 3.8b. It is shown that the sensitivity transfer function achieves the desired +2 slope at low frequencies and that the complementary sensitivity transfer function nominally provides the wanted noise filtering.

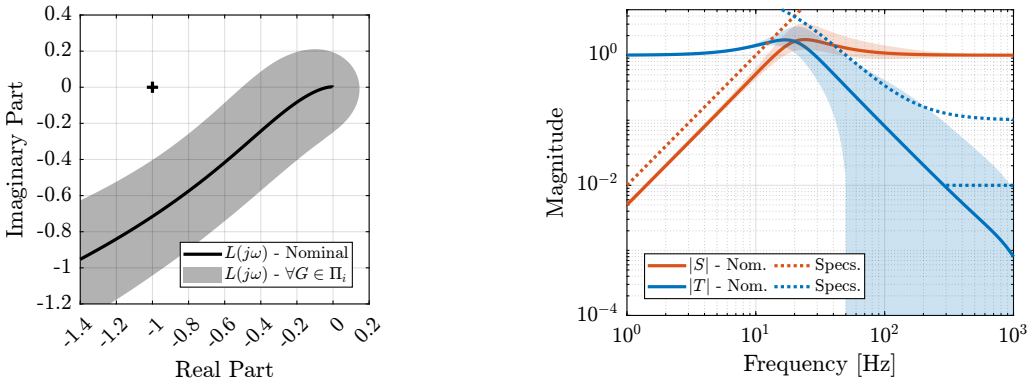

(a) Robust Stability

(b) Nominal and Robust performance

Figure 3.8: Validation of Robust stability with the Nyquist plot (a) and validation of the nominal and robust performance with the magnitude of the closed-loop transfer functions (b)

Conclusion

In this section, a control architecture in which complementary filters are used for closed-loop shaping has been presented. This approach differs from traditional open-loop shaping in that no controller is manually designed; rather, appropriate complementary filters are selected to achieve the desired closed-loop behavior. The method shares conceptual similarities with mixed-sensitivity $\mathcal{H}_\infty$-synthesis, as both approaches aim to shape closed-loop transfer functions, but with notable distinctions in implementation and complexity.

While $\mathcal{H}_\infty$-synthesis synthesis offers greater flexibility and can be readily generalized to MIMO plants, the presented approach provides a simpler alternative that requires minimal design effort. Implementation only necessitates extracting a model of the plant and selecting appropriate analytical complementary filters, making it particularly interesting for applications where simplicity and intuitive parameter tuning are valued.

Due to time constraints, an extensive literature review comparing this approach with similar existing architectures, such as Internal Model Control [56], was not conducted. Consequently, it remains unclear whether the proposed architecture offers significant advantages over existing methods in the literature.

The control architecture has been presented for SISO systems, but can be applied to MIMO systems when sufficient decoupling is achieved. It will be experimentally validated with the NASS during the experimental phase.

Conclusion

Bibliography

[1] X. Li, J. C. Hamann, and J. E. McInroy, "Simultaneous vibration isolation and pointing control of flexure jointed hexapods," in *Smart Structures and Materials 2001: Smart Structures and Integrated Systems*, Aug. 2001 (cit. on pp. 4, 17).

[2] Z. J. Geng, G. G. Pan, L. S. Haynes, B. K. Wada, and J. A. Garba, "An intelligent control system for multiple degree-of-freedom vibration isolation," *Journal of Intelligent Material Systems and Structures*, vol. 6, no. 6, pp. 787–800, 1995 (cit. on p. 4).

[3] C. Wang, X. Xie, Y. Chen, and Z. Zhang, "Investigation on active vibration isolation of a stewart platform with piezoelectric actuators," *Journal of Sound and Vibration*, vol. 383, pp. 1–19, Nov. 2016 (cit. on p. 5).

[4] X. Xie, C. Wang, and Z. Zhang, "Modeling and control of a hybrid passive/active stewart vibration isolation platform," in *INTER-NOISE and NOISE-CON Congress and Conference Proceedings*, Institute of Noise Control Engineering, vol. 255, 2017, pp. 1844–1853 (cit. on pp. 5, 17).

[5] G. Hauge and M. Campbell, "Sensors and control of a space-based six-axis vibration isolation system," *Journal of Sound and Vibration*, vol. 269, no. 3-5, pp. 913–931, 2004 (cit. on pp. 5, 29).

[6] D. Tjepkema, J. van Dijk, and H. Soemers, "Sensor fusion for active vibration isolation in precision equipment," *Journal of Sound and Vibration*, vol. 331, no. 4, pp. 735–749, 2012 (cit. on pp. 5, 6).

[7] M. A. Beijen, D. Tjepkema, and J. van Dijk, "Two-sensor control in active vibration isolation using hard mounts," *Control Engineering Practice*, vol. 26, pp. 82–90, 2014 (cit. on p. 5).

[8] D. Thayer, M. Campbell, J. Vagners, and A. von Flotow, "Six-axis vibration isolation system using soft actuators and multiple sensors," *Journal of Spacecraft and Rockets*, vol. 39, no. 2, pp. 206–212, 2002 (cit. on pp. 5, 17, 29).

[9] X. Yang, H. Wu, B. Chen, S. Kang, and S. Cheng, "Dynamic modeling and decoupled control of a flexible stewart platform for vibration isolation," *Journal of Sound and Vibration*, vol. 439, pp. 398–412, Jan. 2019 (cit. on pp. 5, 17, 29).

[10] J. Bendat, "Optimum filters for independent measurements of two related perturbed messages," *IRE Transactions on Circuit Theory*, 1957 (cit. on p. 6).

[11] F. Shaw and K. Srinivasan, "Bandwidth enhancement of position measurements using measured acceleration," *Mechanical Systems and Signal Processing*, vol. 4, no. 1, pp. 23–38, 1990 (cit. on p. 6).

[12] M. Zimmermann and W. Sulzer, "High bandwidth orientation measurement and control based on complementary filtering," *Robot Control 1991*, Robot Control 1991, pp. 525–530, 1992 (cit. on pp. 6, 7).

[13] H. G. Min and E. T. Jeung, "Complementary filter design for angle estimation using mems accelerometer and gyroscope," *Department of Control and Instrumentation, Changwon National University, Changwon, Korea*, pp. 641–773, 2015 (cit. on p. 6).

[14] W. Hua, "Low frequency vibration isolation and alignment system for advanced ligo," Ph.D. dissertation, stanford university, 2005 (cit. on p. 6).

[15] W. Hua, D. B. Debra, C. T. Hardham, B. T. Lantz, and J. A. Giaime, "Polyphase fir complementary filters for control systems," in *Proceedings of ASPE Spring Topical Meeting on Control of Precision Systems*, 2004, pp. 109–114 (cit. on pp. 6, 7).

[16] A. R. Plummer, "Optimal complementary filters and their application in motion measurement," *Proceedings of the Institution of Mechanical Engineers, Part I: Journal of Systems and Control Engineering*, vol. 220, no. 6, pp. 489–507, 2006 (cit. on pp. 6, 7).

[17] P. Y. C. H. Robert Grover Brown, *Introduction to Random Signals and Applied Kalman Filtering with Matlab Exercises*, 4th ed. Wiley, 2012 (cit. on p. 6).

[18] C. Collette and F. Matichard, "Sensor fusion methods for high performance active vibration isolation systems," *Journal of Sound and Vibration*, vol. 342, pp. 1–21, 2015 (cit. on pp. 6, 30).

[19] Y. K. Yong and A. J. Fleming, "High-speed vertical positioning stage with integrated dual-sensor arrangement," *Sensors and Actuators A: Physical*, vol. 248, pp. 184–192, 2016 (cit. on p. 6).

[20] A.-J. Baerveldt and R. Klang, "A low-cost and low-weight attitude estimation system for an autonomous helicopter," in *Proceedings of IEEE International Conference on Intelligent Engineering Systems*, 1997 (cit. on p. 6).

[21] P. Corke, "An inertial and visual sensing system for a small autonomous helicopter," *Journal of Robotic Systems*, vol. 21, no. 2, pp. 43–51, 2004 (cit. on p. 6).

[22] A. Jensen, C. Coopmans, and Y. Chen, "Basics and guidelines of complementary filters for small uas navigation," in *2013 International Conference on Unmanned Aircraft Systems (ICUAS)*, May 2013 (cit. on pp. 6, 7).

[23] A. Pascoal, I. Kaminer, and P. Oliveira, "Navigation system design using time-varying complementary filters," in *Guidance, Navigation, and Control Conference and Exhibit*, 1999 (cit. on pp. 6, 7).

[24] P. Batista, C. Silvestre, and P. Oliveira, "Optimal position and velocity navigation filters for autonomous vehicles," *Automatica*, vol. 46, no. 4, pp. 767–774, 2010 (cit. on p. 6).

[25] J. van Heijningen, "Low-frequency performance improvement of seismic attenuation systems and vibration sensors for next generation gravitational wave detectors," Ph.D. dissertation, Vrije Universiteit, 2018 (cit. on p. 6).

[26] T. Lucia, "Low frequency optimization and performance of advanced virgo seismic isolation system," Ph.D. dissertation, University of Siena, 2018 (cit. on p. 6).

[27] W. Anderson and E. Fritze, "Instrument approach system steering computer," *Proceedings of the IRE*, vol. 41, no. 2, pp. 219–228, 1953 (cit. on p. 6).

[28] R. G. Brown, "Integrated navigation systems and kalman filtering: A perspective," *Navigation*, vol. 19, no. 4, pp. 355–362, 1972 (cit. on p. 6).

[29] W. T. Higgins, "A comparison of complementary and kalman filtering," *IEEE Transactions on Aerospace and Electronic Systems*, no. 3, pp. 321–325, 1975 (cit. on p. 6).

[30] F. P. N. da Fonseca Cardoso, J. M. F. Calado, C. B. Cardeira, P. J. C. R. Oliveira, et al., "Complementary filter design with three frequency bands: Robot attitude estimation," in *2015 IEEE International Conference on Autonomous Robot Systems and Competitions*, IEEE, 2015, pp. 168–173 (cit. on pp. 6, 13).

[31] S. I. Moore, A. J. Fleming, and Y. K. Yong, "Capacitive instrumentation and sensor fusion for high-bandwidth nanopositioning," *IEEE Sensors Letters*, vol. 3, no. 8, pp. 1–3, 2019 (cit. on p. 6).

[32] T.-J. Yeh, C.-Y. Su, and W.-J. Wang, "Modelling and control of a hydraulically actuated two-degree-of-freedom inertial platform," *Proceedings of the Institution of Mechanical Engineers, Part I: Journal of Systems and Control Engineering*, vol. 219, no. 6, pp. 405–417, 2005 (cit. on p. 6).

[33] D. Stoten, "Fusion of kinetic data using composite filters," *Proceedings of the Institution of Mechanical Engineers, Part I: Journal of Systems and Control Engineering*, vol. 215, no. 5, pp. 483–497, 2001 (cit. on pp. 6, 13).

[34] F. Matichard, B. Lantz, R. Mittleman, et al., "Seismic isolation of advanced ligo: Review of strategy, instrumentation and performance," *Classical and Quantum Gravity*, vol. 32, no. 18, p. 185 003, 2015 (cit. on pp. 6, 13).

[35] T. Dehaeze, M. Vermat, and C. Collette, "Complementary filters shaping using $\mathcal{H}_\infty$ synthesis," in *7th International Conference on Control, Mechatronics and Automation (ICCMA)*, 2019, pp. 459–464 (cit. on pp. 6, 7).

[36] S. Skogestad and I. Postlethwaite, *Multivariable Feedback Control: Analysis and Design - Second Edition*. John Wiley, 2007 (cit. on pp. 12, 24, 29, 32, 33).

[37] K. Furutani, M. Suzuki, and R. Kudoh, "Nanometre-cutting machine using a stewart-platform parallel mechanism," *Measurement Science and Technology*, vol. 15, no. 2, pp. 467–474, 2004 (cit. on pp. 17, 29).

[38] Z. Du, R. Shi, and W. Dong, "A piezo-actuated high-precision flexible parallel pointing mechanism: Conceptual design, development, and experiments," *IEEE Transactions on Robotics*, vol. 30, no. 1, pp. 131–137, 2014 (cit. on pp. 17, 29).

[39] J. McInroy and J. Hamann, "Design and control of flexure jointed hexapods," *IEEE Transactions on Robotics and Automation*, vol. 16, no. 4, pp. 372–381, 2000 (cit. on p. 17).

[40] D. H. Kim, J.-Y. Kang, and K.-I. Lee, "Robust tracking control design for a 6 dof parallel manipulator," *Journal of Robotic Systems*, vol. 17, no. 10, pp. 527–547, 2000 (cit. on p. 17).

[41] H. Abbas and H. Hai, "Vibration isolation concepts for non-cubic stewart platform using modal control," in *Proceedings of 2014 11th International Bhurban Conference on Applied Sciences & Technology (IBCAST) Islamabad, Pakistan, 14th - 18th January, 2014*, Jan. 2014 (cit. on p. 17).

[42] J. Holterman and T. deVries, "Active damping based on decoupled collocated control," *IEEE/ASME Transactions on Mechatronics*, vol. 10, no. 2, pp. 135–145, 2005 (cit. on p. 17).

[43] H. Pu, X. Chen, Z. Zhou, and X. Luo, "Six-degree-of-freedom active vibration isolation system with decoupled collocated control," *Proceedings of the Institution of Mechanical Engineers, Part B: Journal of Engineering Manufacture*, vol. 226, no. 2, pp. 313–325, 2011 (cit. on p. 17).

[44] L. Lei and W. Benli, "Multi objective robust active vibration control for flexure jointed struts of stewart platforms via H_∞ and μ synthesis," *Chinese Journal of Aeronautics*, vol. 21, no. 2, pp. 125–133, 2008 (cit. on p. 17).

[45] J. Jiao, Y. Wu, K. Yu, and R. Zhao, "Dynamic modeling and experimental analyses of stewart platform with flexible hinges," *Journal of Vibration and Control*, vol. 25, no. 1, pp. 151–171, 2018 (cit. on pp. 17, 29).

[46] H. Butler, "Position control in lithographic equipment," *IEEE Control Systems*, vol. 31, no. 5, pp. 28–47, 2011 (cit. on p. 21).

[47] A. M. Rankers, "Machine dynamics in mechatronic systems: An engineering approach.," Ph.D. dissertation, University of Twente, 1998 (cit. on p. 22).

[48] G. F. Lang, "Understanding modal vectors," in *Topics in Modal Analysis & Testing, Volume 10*. Springer, 2017, ch. 8, pp. 55–68 (cit. on p. 23).

[49] A. Preumont, *Vibration Control of Active Structures - Fourth Edition* (Solid Mechanics and Its Applications). Springer International Publishing, 2018 (cit. on p. 23).

[50] S. L. Brunton and J. N. Kutz, *Data-driven science and engineering: Machine learning, dynamical systems, and control*. Cambridge University Press, 2022 (cit. on p. 24).

[51] B. Kouvaritakis, "Theory and practice of the characteristic locus design method," *Proceedings of the Institution of Electrical Engineers*, vol. 126, no. 6, p. 542, 1979 (cit. on p. 25).

[52] M. Hovd, R. D. Braatz, and S. Skogestad, "SVD controllers for $\mathcal{H}_2-$, $\mathcal{H}_\infty-$ and μ-optimal control," *Automatica*, vol. 33, no. 3, pp. 433–439, 1997 (cit. on p. 26).

[53] R. M. Schmidt, G. Schitter, and A. Rankers, *The Design of High Performance Mechatronics - Third Revised Edition*. Ios Press, 2020 (cit. on p. 29).

[54] J. E. Bibel and D. S. Malyevac, "Guidelines for the selection of weighting functions for h-infinity control," NAVAL SURFACE WARFARE CENTER DAHLGREN DIV VA, Tech. Rep., 1992 (cit. on pp. 29, 31).

[55] M. Verma, T. Dehaeze, G. Zhao, J. Watchi, and C. Collette, "Virtual sensor fusion for high precision control," *Mechanical Systems and Signal Processing*, vol. 150, p. 107 241, 2020 (cit. on p. 30).

[56] S. Saxena and Y. Hote, "Advances in internal model control technique: A review and future prospects," *IETE Technical Review*, vol. 29, no. 6, p. 461, 2012 (cit. on p. 38).